University of Zurich[UZH]

Does burn severity in the Arctic tundra vary with vegetation type?

ESS 511 Master's Thesis

Author
Melanie Hodel
18-737-239

Supervised by
Prof. Dr. Gabriela Schaepman
Nils Rietze
Dr. Jakob Assmann (jakob.assmann@uzh.ch)

Faculty representative
Prof. Dr. Gabriela Schaepman

30.04.2024
Department of Geography, University of Zurich

Does burn severity in the Arctic tundra vary with vegetation type?

ESS 511 Master's Thesis

Melanie Hodel

18-737-239

Supervised by

Nils Rietze

Prof. Dr. Gabriela Schaepman-Strub

Dr. Jakob Assmann

30. April 2024

Content

Abbreviations

Abbreviation	Meaning
CBI	Composite Burn Index
DEM	Digital Elevation Model
dNBR	Differenced Normalized Burn Ratio
EFFIS	European Forest Fire Information System
ESA	European Space Agency
FIRMS	Fire Information for Resource Management System
GEE	Google Earth Engine
MTBS	Monitoring Trends in Burn Severity
NBR	Normalized Burn Ratio
NDWI	Normalized Difference Water Index
NIR	Near InfraRed
RGB	Red Green Blue
SWIR	Shortwave InfraRed
TPI	Topographic Position Index

Abstract

The extent of wildfires in the Siberian Arctic has been increasing in recent years, indicating that this region is already undergoing a shift in fire regime as a result of global warming. Major fires occurred in Siberia during the summer months in 2019 and 2020 with exceptionally large burned areas far north in the tundra. This increase in Siberian wildfires causes great concern since tundra fires can induce various ecological consequences such as changes in vegetation composition, permafrost degradation and increased carbon emissions. Little is known about the variation in burn severity in tundra fires. To better understand the spatial pattern of these fires and their correlation with vegetation type, we conducted a burn severity analysis of the two largest northernmost Siberian tundra fires from 2019 and 2020, using Sentinel-2 satellite imagery and the differenced Normalized Burn Ratio (dNBR). Both fires burned predominantly at low severity, with 82% and 84% of the area classified as low burn severity and 18% respectively 16% as high severity. The patch size analysis revealed that the fires created a mosaic of high burn severity patches, with many more small (< 1'000 m^2) patches than large ones (> 10'000 m^2). We detected a significant positive linear relationship between dNBR and elevation respectively Topographic Position Index (TPI), which served as proxies for vegetation types in our study area. However, the low R^2 values (R^2 = 0.1751 and R^2 = 0.1741) and the large scatter of the dNBR values suggested that burn severity cannot be adequately explained by TPI and elevation, implying that other factors such as fire residence time, fire weather or fuel moisture likely determined the burn severities. Further analysis of the burn severity in Siberian tundra wildfires require more in-situ data to accurately calibrate and validate the severity classification. Nevertheless, more comprehensive burn severity assessments of Siberian tundra wildfires using dNBR are needed and could explore the connection between dNBR and post-fire vegetation dynamics.

1 Introduction

The Arctic is warming at a rate almost four times as fast as the global average (Rantanen et al., 2022), a process called Arctic Amplification (Serreze & Francis, 2006). In a warming Arctic, extreme weather conditions (Flannigan et al., 2013), drier fuels (Flannigan et al., 2016) and lightning (Chen et al., 2021b) become more frequent and as a result, Arctic wildfire activity is expected to increase in the future (McCarty et al., 2021). An increase in wildfires in high latitudes causes great concern (Mack et al., 2011) because tundra soils have the highest soil carbon density among all biomes and store more than 13% of the world's soil carbon (Post et al., 1982). Tundra fires could therefore release a significant amount of carbon, ultimately diminishing the carbon storage in this region and leading to higher CO_2 concentrations in the atmosphere (Mack et al., 2011). For instance, the Anaktuvuk River fire produced carbon emissions that were roughly corresponding to the annual carbon sink of the whole tundra biome (Mack et al., 2011). This is a major problem in particular because high carbon emissions contribute to further warming, which in turn causes more wildfires and permafrost thaw, creating a positive feedback that amplifies global warming (Mack et al., 2011; Natali et al., 2021). An intensification of Arctic wildfires therefore jeopardizes the achievement of the Paris Climate Agreement (Natali et al., 2021).

In 2019 and 2020 major fires occurred in eastern and central Siberia, with exceptionally large burned areas and enhanced fire intensity far north in the tundra, whereby a substantial part of peatlands was affected (Descals et al., 2022; Scholten et al., 2022). The combination of an early snowmelt and arctic front jets, as well as hot and dry conditions contributed to these intense wildfires in the northern tundra (Scholten et al., 2022). The upward trend in yearly burned area in the Siberian Arctic indicates that, as a result of global warming, this region is already undergoing a shift in fire behaviour (Descals et al., 2022). Under representative concentration pathway 4.5 and 8.5 scenarios, the annually burned area in the Siberian Arctic has been estimated to vary between 0.5 and 2.5 million hectares by 2050, leading to an average carbon emission of 37.8 teragrams per year (Descals et al., 2022).

Despite an increase in carbon emissions, tundra fires can lead to increased thaw depths and changes in the composition and structure of vegetation (Racine et al., 2004; Rocha et al., 2012; Rocha & Shaver, 2011a; Rocha & Shaver, 2011b). In Alaska, shrubs occurred more frequently after fire, while other species such as mosses and lichens showed slight to no regeneration at

all (Racine et al., 2004). There is also a sparking concern that tundra fires could promote treeline advancement (Racine et al., 2004). However, the magnitude of carbon emissions, thaw depths and vegetation change after a fire depends on the burn severity (Racine et al., 2004; Rocha & Shaver, 2011a; Rocha & Shaver, 2011b). In the literature, there are several different definitions of burn severity (Key & Benson, 2006; Lentile et al., 2006). Unfortunately, the term is not used consistently and is often confused with other terms such as fire severity or fire intensity (Key & Benson, 2006; Lentile et al., 2006). In the context of this master thesis, burn severity refers to the dNBR index assessing the degree of ecological change resulting from a fire, with regard to how many plants survive respectively die, the quantity of consumed biomass and the extent of organic layer burning (Allen & Sorbel, 2008; Key & Benson, 2006). Because of this strong link to the effects of fires, burn severity is a fundamental fire variable and crucial for fire and resource management (Allen & Sorbel, 2008; Chen et al., 2020a). Burn severity maps are also of great importance for research and monitoring, as they help modelling the fire impacts on vegetation, fauna populations, permafrost, and carbon emissions (Allen & Sorbel, 2008; Rocha & Shaver, 2011a).

Fires often do not burn uniformly across the landscape (Allen & Sorbel, 2008). The appearance, the size and the burn severity of a fire are determined by climate and the heterogeneity of the landscape, such as topography and the prevalent vegetation (Allen & Sorbel, 2008). For example, the amount of wood or biomass destroyed during a fire is not homogeneously distributed across the fire scar but can vary greatly depending on the species, as certain species are more fire-resistant in comparison to others (Key & Benson, 2006). Consequently, during a fire, certain parts are left unaffected, while other areas are severely altered due to charring and prolonged burning of the vegetation cover and soil layer (Allen & Sorbel, 2008). This fluctuating burn severity creates a heterogeneous spatial pattern, a so-called “fire mosaic”, demonstrating the complexity of a burned area (Allen & Sorbel, 2008; Key & Benson, 2006). Both so-called top-down factors such as climate and weather as well as bottom-up factors like vegetation and topography shape the burn severity of a fire (Wu et al., 2013). Determining the influence of topography and vegetation on the burn severity of a fire offers a solid foundation for fire management strategies aimed at mitigating devastating wildfires (Wu et al., 2013). Especially in the wake of climate warming, it is crucial to investigate why certain fires have an increased burn severity (Wu et al., 2013). To this date, however, there is not much knowledge on the influence of vegetation on burn severity in Arctic tundra fires, and especially not in the

Siberian tundra in the far North-East. The remote site and the limited duration of the growing season imposes significant constraint on gathering solid field observations of the fire regimes in the Arctic (Allen & Sorbel, 2008; Kolden & Rogan, 2013).

Remote sensing therefore plays a crucial role in the observation and analysis of burn severity at both the global and local level, as it allows for the detection of big, inaccessible and remote fires (Allen & Sorbel, 2008; Key & Benson, 2006; Llorens et al., 2021). Burn severity can be approximated using the differenced Normalized Burn Ratio (dNBR), a spectral index that can be calculated from readily available satellite data such as Sentinel-2 or Landsat imagery (Key & Benson, 2006; Llorens et al., 2021). Even though most studies use common burn severity classes such as unburned, low, moderate and high severity, they rely on field observations for accurate burn severity discrimination, limiting their applicability in difficult to reach areas (Allen & Sorbel, 2008; Jones et al., 2009; Kolden & Rogan, 2013). Therefore, it is crucial to study how the dNBR itself relates to the vegetation and topography of the fires in the Siberian tundra, where we lack in-situ observations of burn severity.

This thesis focused on the two largest, northernmost tundra fires in northeastern Siberia in 2019 and 2020. We addressed the following questions:

1) What was the extent of the burn severities of the tundra fires in the study area in Siberia in 2019 and 2020?
2) How did the high severity burns vary within and between the fire scars?
3) Is burn severity related to vegetation type?

To tackle these questions, we used Sentinel-2 satellite imagery to determine the spatial extent of high and low burn severities of the tundra fires. Second, we extracted patch sizes of high burn severity patches to investigate their variation within and between fire scars and third, we analysed the relationship between vegetation types and dNBR using linear regression. The aim of this master's thesis was to attain a more detailed understanding of the extensive northeastern Siberian tundra fires in 2019 and 2020 and their relationship with vegetation, as well as a better prediction of fire effects in the Siberian Arctic, which helps to find better management practices to counteract the fires and their associated negative effects such as carbon dioxide emissions and amplified global warming.

2 Data and methods

2.1 Study area

The study area is located at high latitudes in the northeastern part of Sibera, Russia (Figure 1), in the region of the Kytalyk National Park (70°49'N, 147°28'E). This national park is situated 50 – 80 m asl within the lower reaches of the Indigirka River basin, Republic of Sakha (Yakutia) (UNESCO, 2023). Alongside the Indigirka River, there are several tributaries and numerous oval and roundish thermokarst lakes (UNESCO, 2023). The entire study area is underlain by continuous permafrost (Holloway et al., 2020; Talucci et al., 2022). The region is characterized by plateaus, pingos and ridges that elevate from the circumjacent wet tundra and harbour vegetation adjusted to dry conditions (UNESCO, 2023). The study area involves variations in elevation from about 0 to 55 m.

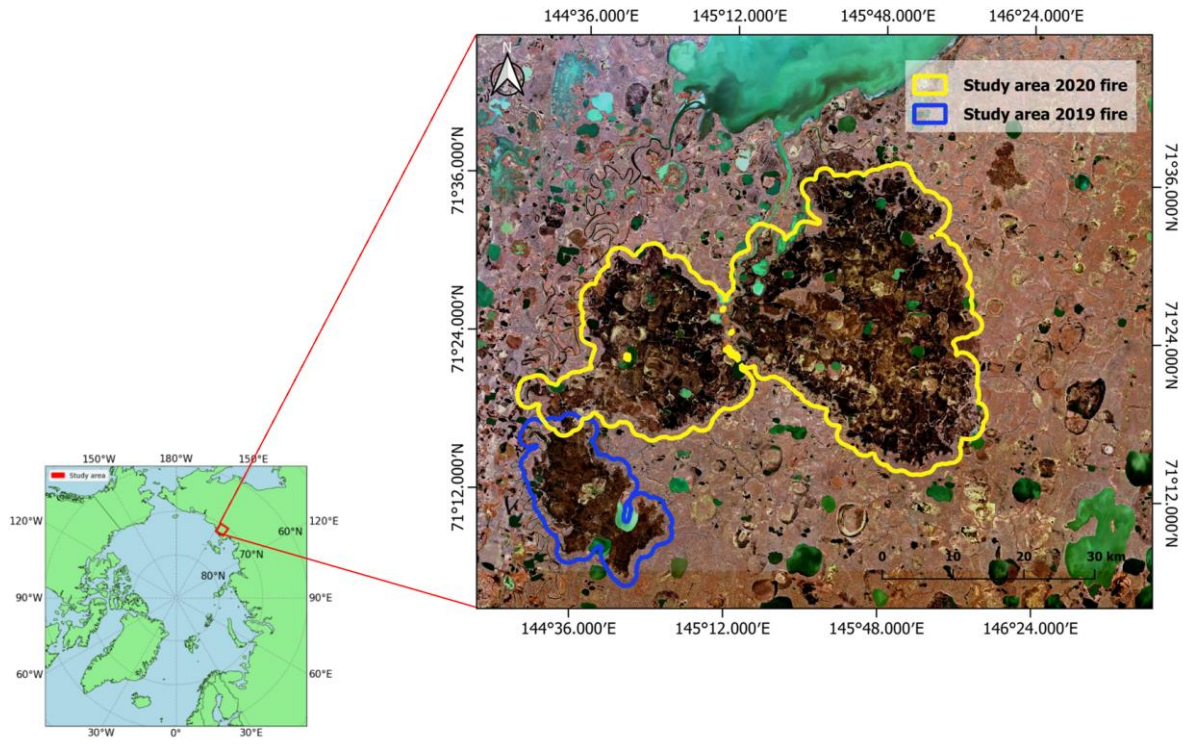

Figure 1: Overview map of the study area location (red rectangle) in the region of the Kytalyk National Park, in northeastern Siberia, Russia. On the right side a zoomed-in map where the burned area is visible. The blue outline shows the study area of the 2019 fire, and the yellow outline the study area of the 2020 fire, which we delineated using a 1.2 km buffer around the vectorized burned area from Descals et al. (2022). The background map is retrieved from Google Earth Engine provided by the European Space Agency (ESA, 2023).

The vegetation in the study area is characterized by dwarf-shrubs, moist-tussock-sedge, moss tundra and low-shrub tundra, following the Circumpolar Arctic Vegetation Map classification (Blok et al., 2011; Walker et al., 2005).

The area consists of three main landform types: drained thaw lake basins, active river floodplain with river terrace, and Yedoma remnants (van Huissteden et al., 2021). The Yedoma remnants are an ice-rich permafrost deposit from the Pleistocene (Schirrmeister et al., 2013) and have the form of a plateau with a flat surface area that are typically well-drained, covered mainly by tussock-tundra (Khitun et al., 2020; van Huissteden et al., 2021). In the drained thaw lake basins, the landscapes consist of polygon complexes, where wet depressions are primarily dominated by sedges, while the high centres of polygons are dominantly covered by shrubs and lichen (Khitun et al., 2020; Parmentier et al., 2011; van Huissteden et al., 2021).

We concentrated our analysis on the two largest, northernmost burns that occurred in 2019 and 2020. Descals et al. (2022) have already mapped all burned areas in the Siberian Arctic from 1981 to 2020, including the northeastern Siberian tundra fires from 2019 and 2020. Therefore, we used their dataset to increase the validity of the burn severity analysis and to limit our study area to a region, where other studies already determined the occurrence of a fire. A buffer of 1.2 km around the fire scar was included to leave some space for unburned areas surrounding the scar and to capture potentially burned areas that Descals et al. (2022) did not detect (Figure 1).

2.2 Satellite image processing

2.2.1 Burn severity assessment

The burn severity analysis was done in Google Earth Engine (GEE), a cloud-based platform that allows large-scale processing and analysis of satellite imagery (GEE, 2023). We used atmospherically corrected Sentinel-2 Level-2A and top of atmosphere reflectance Level-1C satellite images to calculate the dNBR for our burn severity analysis (ESA, 2023). The data was provided by the European Space Agency (ESA) and directly assessed through GEE (ESA, 2023).

The burn severity in the study area was determined using the differenced Normalized Burn Ratio (dNBR) according to Key & Benson (2006). The dNBR is a spectral index to map burned areas and burn severity by generating a numeric scale measuring the extent of change occurring in the environment after a fire (Key & Benson, 2006). We calculated the NBR as follows:

$$NBR = \frac{\rho_{NIR} - \rho_{SWIR}}{\rho_{NIR} + \rho_{SWIR}} = \frac{B8A - B12}{B8A + B12}$$

where ρ refers to the atmospherically corrected surface reflectance in the near-infrared (NIR) respectively the shortwave-infrared (SWIR) spectral range. In the case of Sentinel-2 Level-2A data in GEE, this corresponds to band 8A and band 12 (Table 1).

Table 1: Description of the different bands used for the NBR calculation, with resolution in meters and wavelength in nanometers. S2A and S2B refer to the twin satellites of the Sentinel-2 mission, Sentinel-2A and Sentinel-2B, that have a revisit rate of about 3 days at Kytalyk (ESA, 2023).

Band	Description	Resolution [m]	Wavelength [nm]
B8A	Red Edge 4	20	864.8 (S2A) / 864 (S2B)
B12	SWIR2	20	2202.4 (S2A) / 2185.7 (S2B)

The NBR corresponds to the normalized difference between the near-infrared (NIR) and the shortwave-infrared (SWIR) band and was originally developed for the Landsat thematic mapper instrument (Key & Benson, 1999; López García & Caselles, 1991). However, the multispectral instrument on the Sentinel satellites offers an alternative data source with higher resolution (Alcaras et al., 2022; Liu et al., 2023; Llorens et al., 2021).

The NIR reflectance increases with leaf area and vegetation productivity, while the SWIR band has a high reflectance over dry and non-vegetated terrain, and correspondingly a low reflectance over wet areas and lush vegetation. After the occurrence of a wildfire, the area generally has a lower vegetation density and vitality, which manifests in a lower reflectance in the NIR. At the same time, there is increasingly more soil exposed, drier substrates, and scorched fuels, resulting in an increased reflectance of SWIR. Accordingly, the NIR reflectance decreases while the SWIR reflectance increases going from healthy to burned vegetation (Figure 6 in Appendix). These two bands therefore provide a very good discrimination between unburned and burned areas, as well as information on the degree of burn severity. The NBR spectral index can take a value from -1 to +1, whereby NBR values close to zero to highly negative indicate burned areas. The difference between NIR and SWIR surface reflectance is divided by the sum of these two bands to correct for topographical and solar illumination effects (Key & Benson, 2006).

The NBR was calculated for the post and the pre-burn image. In a next step, the differenced NBR (dNBR) was calculated by subtracting the post-burn image from the pre-burn image (Key & Benson, 2006) to carry out a bi-temporal assessment, which yields more accurate results than the NBR alone (Alcaras et al., 2022; Chen et al., 2020b).

$$dNBR = NBR_{pre-burn} - NBR_{post-burn}$$

The pre- and post-fire NBR images are subtracted from each other to separate the burned area from its surrounding, unburned land (Key & Benson, 2006). The dNBR values were multiplied by 10^3 to follow the convention set by Key and Benson (2006). In theory, the dNBR values can range from -2'000 to +2'000 (Key & Benson, 2006). Under the assumption that the unburned area has similar moisture levels and phenology in the pre- and post-burn image, the dNBR values of unburned areas will be close to zero, while the burned areas take on highly positive values depending on the degree of burn severity (Key & Benson, 2006). In reality, the dNBR values often do not fall below -550 or exceed +1'350 (Key & Benson, 2006). Values outside this range tend to be misclassifications related to water bodies, clouds or missing values in one of the pre- or post-burn images (Alcaras et al., 2022; Key & Benson, 2006). We identified a total of 10 pixels that fell outside of this typical range for dNBR values. A manual inspection showed that these pixels were all in water bodies. Therefore, we excluded these pixels from further analyses.

Although there are many different indices for burn severity assessment, the dNBR performs well in comparison to others (Epting et al., 2005) and is the most commonly used index, applied in a wide range of ecosystems such as boreal forests, mediterranean forests and shrublands (Allen & Sorbel, 2008; Llorens et al., 2021; López García & Caselles, 1991). The index is also utilized by the European Forest Fire Information System (EFFIS) (https://effis.jrc.ec.europa.eu/) and the multiagency program Monitoring Trends in Burn Severity (MTBS), which maps fires and burn severity across the United States (https://www.mtbs.gov/). It is a standard approach that allows the comparison of different burns over space and time (Key & Benson, 1999; Key & Benson, 2006). The applicability of the dNBR for the Arctic tundra has been tested and approved by several studies. For instance, Allen & Sorbel (2008) have validated the suitability of the dNBR for Arctic tundra burn severity mapping demonstrating good alignment with in-situ ground measurements. Also, Jones et al. (2009) and Kolden & Rogan (2013) used the dNBR as a burn severity measure for tundra fires and showed high correlation between dNBR and field data (correlation coefficient $R^2 = 0.814$ and $R^2 = 0.82$).

2.2.2 Image acquisition and preprocessing

The dates selected for the pre- and post-burn images are of great importance, as they are the main cause of inadequate outcomes (Key & Benson, 2006; Loboda et al., 2013). Ideally, the unburned areas are captured under similar environmental conditions, in order to display only changes that were induced by the fire (Key & Benson, 2006). However, this is often not the case since unburned areas change over time as a result of productivity and soil moisture variations (Key & Benson, 2006). Accordingly, it is recommended to acquire pre- and post-burn images that have similar phenology and moisture level (Key & Benson, 2006). At the same time, the satellite imagery should have as little cloud cover as possible, because clouds tend to be misclassified as burned areas (Alcaras et al., 2022). The selection of the dates for the post-burn image also depends on whether an initial or extended assessment of the burn severity is performed (Key & Benson, 2006). An initial assessment seeks to capture the most immediate burn impacts and therefore the post-burn image is taken as soon as the fire is extinguished (Key & Benson, 2006). In contrast, for the extended assessment, the post-burn image is taken in the subsequent growing season to capture vegetation regeneration and delayed vegetation dieback (Key & Benson, 2006).

In order to determine the best possible point in time for pre- and post-burn data that fulfil all of the above-mentioned criteria, we used the global fire map from the Fire Information for Resource Management System (FIRMS) (https://firms.modaps.eosdis.nasa.gov/map/). The FIRMS database revealed that there were recurring fires in the study area form July 11th to September 5th in 2019 and from June 14th to August 7th in 2020. We tested various pre- and post-burn image date combinations, which included both initial and extended assessments (Figure 7 and 8 in Appendix). Ideally, an extended assessment would be carried out, where the post-burn image is taken in the growing season from the following year, providing maximum contrast between burned and unburned areas (Key & Benson, 2006). However, cloud cover and smoke from the fires posed an issue, especially because August 2020 was overcast throughout. Ultimately, it was necessary to carry out an initial assessment, and we acquired post-burn images as close as possible to the fire date and pre-burn images from the same season one year before (Table 2). Only this way it could be ensured the pre- and post-burn images were taken from the same season at a similar time, ensuring similar moisture level and phenology (Chen et al., 2020a; Key & Benson, 2006). An initial assessment also ensured that not too many years have passed between pre- and post-burn images and thus not too much

regeneration has already taken place, which would have dampened the dNBR signal (López García & Caselles, 1991). The MTBS generally uses an initial assessment for grasslands and low biomass shrublands, while an extended assessment is conducted for forests and shrublands high in biomass (https://burnseverity.cr.usgs.gov/products/mtbs), which supports our decision.

Table 2: Chosen dates for pre- and post-burn images for each fire, with spatial resolution in meters.

Fire year	Pre-burn image	Post-burn image	Spatial resolution
2019	2018-09-09 (Sentinel2-L1C)	2019-09-13 (Sentinel2-L2A)	20 m
2020	2019-09-13 (Sentinel2-L2A)	2020-09-11 (Sentinel2-L2A)	20 m

All images were Sentinel-2 Level-2A data, which represent surface reflectance images that are already atmospherically corrected, except for the pre-burn image of the 2019 fire, which was only in the form of Sentinel-2 Level-1C available, representing the top of atmosphere reflectance (ESA, 2023). Therefore, we atmospherically corrected this image ourselves prior to performing the burn severity assessment using Sen2cor v2.11, a tool which generates Sentinel-2 Level-2A products from input Level-1C data (https://step.esa.int/main/snap-supported-plugins/sen2cor/). The atmospheric correction comprises the adjustment of various atmospheric phenomena, such as the absorption and scattering resulting from aerosols, air molecules and atmospheric gases, like water vapor, oxygen and ozone (ESA, 2023).

As all images were completely cloud-free, we did not apply a cloud mask (Alcaras et al., 2022).

2.2.3 Water mask

Before the NBR calculations were carried out, we masked out all water surfaces since water bodies tend to be misclassified as burned areas (Alcaras et al., 2022). This was done using the Normalized Difference Water Index (NDWI) according to McFeeters (1996), which was calculated as follows:

$$NDWI = \frac{\rho_{Green} - \rho_{NIR}}{\rho_{Green} + \rho_{NIR}} = \frac{B3 - B8}{B3 + B8}$$

where ρ refers to the atmospherically corrected surface reflectance in the green respectively the near-infrared (NIR) spectral range. In the case of Sentinel-2 Level-2A data in GEE, this corresponds to band 3 and band 8.

The NDWI values have a range from -1 to +1 (McFeeters, 1996). Water bodies tend to be represented by positive values, whereas negative values show vegetation and soil (McFeeters, 1996). Therefore, we used a default threshold of 0 to mask out the thermokarst lakes and rivers in our study area.

2.2.4 Burn severity classification

To classify the dNBR values into different classes such as unburned, low and high burn severity, on-site ground measurements of burn severity is commonly used, a so-called Composite Burn Index (CBI) (Allen & Sorbel, 2008; Jones et al., 2009; Key & Benson, 1999; Loboda et al., 2013). The CBI method divides plots into different strata and visually estimates their burn severity based on selected criteria (Key & Benson, 2006). Subsequently, these estimations are summarized into an overall rating (Key & Benson, 2006). However, no field observations of the CBI were available for the study area.

Key & Benson (2006) provide example thresholds for different severity levels (Table 6 in Appendix), which are used by the EFFIS and the MTBS. However, these are not suitable for all scenarios, as the thresholds are flexible and can vary by $\pm$ 100 depending on the season and time of the acquired satellite imagery and whether an initial or extended assessment is conducted (Key & Benson, 2006).

For that reason, we used image-based training polygons to determine the thresholds for the classification. At total of 15 training polygons and 5 validation polygons of identical size (47 pixels) were visually selected for each burn severity class for each fire (unburned, low and high burn severity). We determined the locations of the polygons using the RGB and SWIR composite images, where the burned areas were clearly visible. To ensure an optimal representation of different burn severities, we delineated an even amount of polygons per burn severity. Then the dNBR range of the training polygons of the three burn severity classes were plotted together in a histogram for each fire (Figure 2). We removed the upper and lower 10% of each distribution to improve the threshold identification between the three classes, since they partially overlapped. The mean between the maximum value of the unburned distribution and the minimum value of the low burn severity distribution, respectively the maximum value of the low burn severity and the minimum value of the high burn severity distribution were then used as the thresholds separating unburned from low severity and low severity from high severity (Table 3).

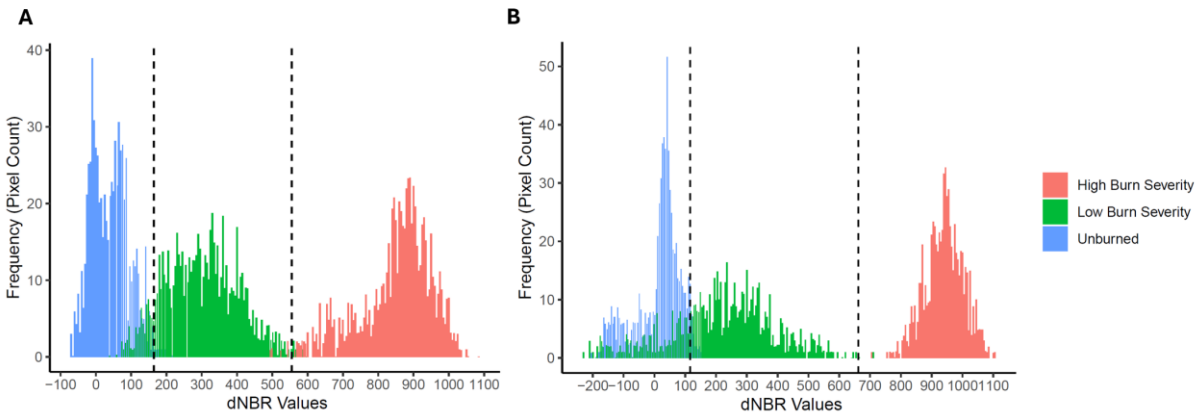

Figure 2: Histogram of the dNBR distributions from the training polygons for the three different burn severity classes (unburned, low burn severity and high burn severity) for A) the 2019 fire and B) the 2020 fire. The black dotted lines show the thresholds separating the burn severity classes. In A) the thresholds are at 164 and 555 and in B) the thresholds are at 116 and 662.

The results of the classification were validated using a confusion matrix (Figure 9 in Appendix), where the validation polygons were compared to the classified image. The confusion matrix yields three different accuracy outcomes: Producer's accuracy, user's accuracy and overall accuracy (Fung & Ledrew, 1988). The overall accuracy shows what proportion of the map was correctly classified (Fung & Ledrew, 1988), which was 98.8% and 82.3% for the 2019 and the 2020 fire. The producer's accuracy illustrates "the number of correctly classified pixels within a specific class divided by the total number of reference pixels for that class" (Fung & Ledrew, 1988). The producer's accuracy of the unburned class was 99.6% and 94.7% for the 2019 and the 2020 fire. For the low burn severity class, producer's accuracy was 96.7% and 52.3% while for the high severity class it reached 100% for both fires. In contrast to that, the user's accuracy demonstrates "the number of correctly classified pixels within a specific class divided by the total number of pixels that were classified as that class" (Fung & Ledrew, 1988). The user's accuracies were 97.6% and 66.5% for the unburned class, 99.6% and 90.8% for the low burn severity class and 99.2% and 100% for the high burn severity class for the 2019 and 2020 fire.

Table 3: Burn severity classification with the used dNBR ranges for the different burn severity classes for the 2019 and the 2020 fire.

Burn severity class	**dNBR range 2019 Fire**	**dNBR range 2020 Fire**
Unburned	-550 ≤ to > 164	-550 ≤ to > 116
Low burn severity	164 ≤ to > 555	116 ≤ to > 662
High burn severity	555 ≤ to > 1350	662 ≤ to > 1350

2.3 Statistical analysis

2.3.1 Variation of the high severity burns within and between the fire scars

To characterize the variation of the high severity burns within and between the fire scars, we performed a patch analysis on the classified burn severity raster in RStudio using the *landscapemetrics* package (Hesselbarth et al., 2019). The *landscapemetrics* package encompasses several functions to compute commonly used landscape metrics on patch-, class- and landscape-level (Hesselbarth et al., 2019). Here we used the *lsm_p_area* command at patch-level to calculate the area of every high severity patch within the 2019 and 2020 fire scars, whereby a patch is defined as connected adjacent pixels belonging to the same burn severity class (Hesselbarth et al., 2019). For patch delineation we used the default queen's case (8 neighbouring cells) (Hesselbarth et al., 2019).

The next step was to test whether there was a significant difference in the frequency distribution of the high burn severity patch sizes between the 2019 and 2020 fire. To this end, we log-transformed the patch size and took a random sample of 2'000 high severity patch size values for each year which were then displayed in a boxplot (Figure 10 in Appendix). Since the data were not normally distributed but right-skewed, we performed a Wilcoxson rank-sum test, also referred to as Mann-Whitney-U-Test (McKnight & Najab, 2010). The Wilcoxson rank-sum test is the "non-parametric equivalent to the parametric t-test" but makes no specific assumption about the distribution (McKnight & Najab, 2010). This statistical test assesses whether "the central tendencies of two independent samples differ", respectively whether the two samples are "from the same population" (McKnight & Najab, 2010; University of Zurich, 2023). To this end, the values from both samples are combined and ranked from 1 to N (the total sample size) and then the rank scores are summed up by sample, resulting in a rank sum for each sample (McKnight & Najab, 2010).

2.3.2 Burn severity relation to vegetation type

In order to test if there is a relationship between burn severity and vegetation type, we used the Arctic Digital Elevation Model (DEM) available in GEE, provided by the Polar Geospatial Center (Porter et al., 2018). As there exists no vegetation map with sufficient resolution in our study area, elevation and TPI (Topographic Position Index) served as a proxy for the local vegetation.

The TPI can distinguish between upland and lowland areas (Weiss, 2001) which correspond well with the main landforms in the study area (van Huissteden et al., 2021). These landforms are representative for the vegetation types in our study area (Khitun et al., 2020; Parmentier et al., 2011; van Huissteden et al., 2021). The TPI identifies these landforms by comparing the elevation of every pixel to the average value of its adjacent, neighbouring pixels (Weiss, 2001). The size of the neighbourhood significantly impacts the calculation. For example, using a radius of 100 m reveals local fine-scale topographic features, while a radius of 2'000 m shows large-scale topographic features (Weiss, 2001). We used a focal window with a side length of 500 m in order to be able to capture the large landform types in our study area such as drained thaw lake beds and Yedoma ridges. A TPI around zero corresponds to flat areas, a negative TPI represents the drained thaw lake basins and a positive TPI depicts the Yedoma ridges (Weiss, 2001).

Subsequently, the elevation and TPI map were overlaid with the dNBR map and random points were generated within each fire scar. However, the elevation and TPI histograms revealed that not all elevation and TPI values occur with the same frequency across the study area (Figure 11 and 12 in Appendix). For instance, high elevation values (> 30 m) occur less frequently than moderate elevation values (15 m). To ensure that the random points are distributed more or less equally across the entire elevation and TPI spectrum, we divided the TPI and elevation maps into smaller bins (Table 7 in Appendix) and sampled 100 random points within each predefined elevation and TPI range. To ensure that the random points are representative of the dNBR values occurring within the elevation and TPI ranges, the dNBR distribution of the 100 random points was plotted against the dNBR distribution of all pixels within the respective elevation and TPI range (Figure 13 and 14 in Appendix).

Finally, elevation, TPI and dNBR values were extracted at these random points and a linear regression was conducted to test whether there is a significant relationship between dNBR and elevation and dNBR and TPI.

3 Results

3.1 Extent of the burn severities of the tundra fires in the study area in 2019 and 2020

The different burn severity levels were heterogeneously distributed for the 2019 and the 2020 fires, showing the complexity of these fires (Figure 3). In both years there is a prevalence of the low burn severity. A roughly equal proportion of the fire scars burned with low severity in both years, with 81% in 2019 and 84% in 2020. Only 19% respectively 16% of the fires burned with high burn severity, highlighting the predominance of the low burn severity class. Although the 2020 fire was overall about five times larger than the 2019 fire, the ratio between low and high severity was similar in both years, with 4:1 in 2019 and about 5:1 in 2020.

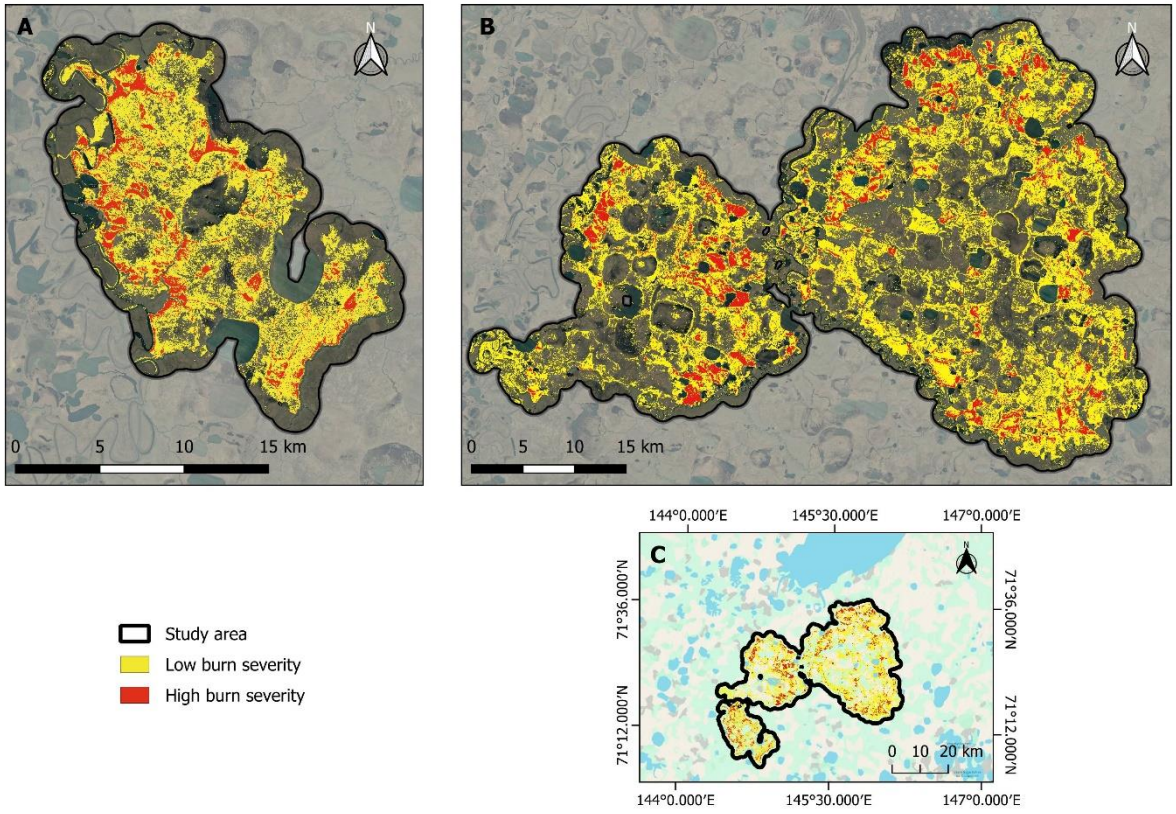

Figure 3: Burn severity map for A) the 2019 fire, where a low burn severity corresponds to a dNBR range from 164 ≤ to > 555 and a high burn severity to a range from 555 ≤ to > 1350, and for B) the 2020 fire, where a low burn severity corresponds to a dNBR range from 116 ≤ to > 662 and a high burn severity to a range from 662 ≤ to > 1350. We delineated the study area (black outline) using a 1.2 km buffer around the vectorized burned area from Descals et al. (2022). C) Map showing the two burned areas side by side. The background maps are retrieved from map data ©2015 Google and are semi-transparent to enhance the study area in the imagery.

In 2019, an area of about 101 km^2 burned at low severity, while the high severity burns covered an area of about 24 km^2 (Table 4). For the 2020 fire the low severity burns comprised an area

of 539 km^2 and the high severity burns covered an area of 106 km^2. In total, the two largest northernmost tundra fires in 2019 and 2020 burned an area of 125 km^2 and 645 km^2 respectively.

Table 4: Extent of burn severities and the total burned area of the tundra fires in the study area in northeastern Siberia in 2019 and 2020, expressed in square kilometer [km^2] and percentage [%].

	2019 Fire		2020 Fire	
	Area [km^2]	**Percentage [%]**	**Area [km^2]**	**Percentage [%]**
Low burn severity	100. 6	81	539.1	84
High burn severity	24.1	19	105.9	16
Total	124.7	100	645	100

The burn severity map also reveals that not the entire area within the fire scars has burned, but that there are always patches that remained unaffected by the fire. The extent and the spatial pattern of the low and high severity burns was partially confined by the thermokarst lakes in the study area, as well as adjacent rivers. Moreover, the high burn severity areas seem to visually cluster in space.

3.2 Variation of the high severity burns within and between the fire scars

The fires showed similar percentages of the high burn severity areas, but we found differences in the patch sizes, revealing variation in high severity patch sizes within fire scars.

The size of the high severity patches ranged from 400 m^2 to 2.06 km^2 (Table 5). There were only a few large patch sizes (> 10^5 m^2) (less than 10% of the total high severity area) and a lot of small-medium sized ones (< 10^5 m^2) (more than 90%) (Figure 4). The larger the patch size, the smaller the frequency. The smallest patch size was 400 m^2, which corresponds to the maximum spatial resolution of the image (20 m pixel resolution of Sentinel-2 imagery).

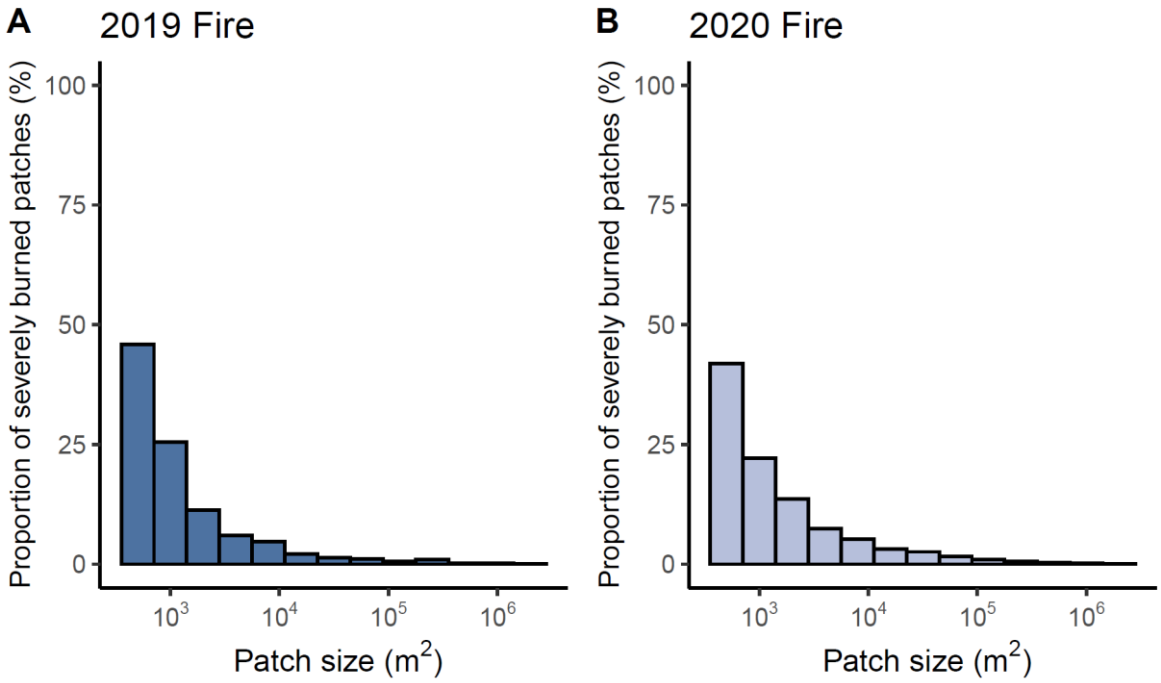

Figure 4: Distribution of the high burn severity patch sizes, expressed in percentage (%) for A) the 2019 fire and B) the 2020 fire.

The distribution of the high burn severity patches looks very similar for both years, but they differ statistically (Mann-Whitney-U statistic W = 1859687, p-value = 5.675 * 10^{-5}, Figure 10 in Appendix). In 2020, the frequency of the patch sizes is a lot higher (Figure 15 in Appendix) because the total area burned in 2020 is larger than in 2019. Moreover, the mean patch area of the 2020 fire is slightly higher, and the maximum patch size with an area of 2.06 km^2 is bigger compared to the 1.75 km^2 of the 2019 burn (Table 5).

Table 5: High burn severity patch area statistic for the 2019 and 2020 fire, where n = number of patches, min = minimum patch area, max = maximum patch area, median = median value of the patch area, and mean = arithmetic mean of the patch area.

		Patch area			
	n	**Min**	**Max**	**Median**	**Mean**
2019 Fire	2'717	400 m^2	1.75 km^2	800 m^2	8'877 m^2
2020 Fire	8'585	400 m^2	2.06 km^2	800 m^2	12'336 m^2

3.3 Burn severity relation to vegetation type

For both variables, elevation and TPI, there is a slightly positive relationship with dNBR, demonstrating that there is a small tendency that with higher elevation and TPI, burn severity is higher (Figure 5). However, the scattering is very large, and we find low and high burn severity at low and high elevations and TPI values. Especially at higher elevation and TPI values, the dNBR values span a wide range from very low to very high burn severities.

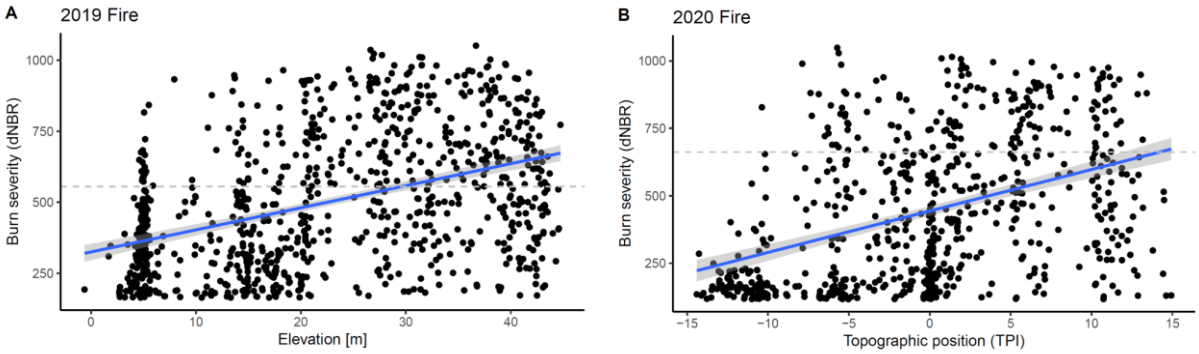

*Figure 5: A) Relation between burn severity (dNBR) and elevation and B) burn severity (dNBR) and topographic position (TPI). The black dots represent random samples within the fire scars. The blue lines show the linear regression line fitted to the data with a confidence interval (R^2 = 0.1751, p-value = < 2.2 * 10^{-16} for A) and R^2 = 0.1741, p-value = < 2.2 * 10^{-16} for B). The grey dashed lines illustrate the thresholds between low and high burn severity (dNBR threshold at 555 for A) and dNBR threshold at 662 for B). The other two relationship plots for each respective fire scar are shown in Figure 16 in the Appendix.*

Although the positive linear relationship between dNBR and elevation and dNBR and TPI is significant (p-value < 0.01), the R^2 values are very low for both fires (R^2 = 0.1751 and R^2 = 0.1741). However, even though the relationships are weak (low R^2), there seems to be a clear group at low elevations and topographic positions that have really low burn severities.

In addition, we also tested the relationship between dNBR and slope, as well as dNBR and aspect (Figure 17 in Appendix). The linear regression revealed no significant relationship between dNBR and aspect, with both low and high burn severities occurring irrespective of the aspect. Concerning the slope, the fitted values showed heteroscedasticity, and therefore we did not apply a linear model to test for the significance of the relationship. Nevertheless, the high burn severity seems to visually cluster around a slope of 5°, while above and below that threshold burn severity tends to decline.

4 Discussion

4.1 Extent of the burn severities of the tundra fires in the study area in 2019 and 2020

Distinguishing between the unburned and low severity classes is challenging due to significant overlap in their dNBR values. This limited accuracy of the burn severity classification is visible in the confusion matrix (Figure 9 in Appendix). The unburned class of the 2020 fire had a user's accuracy of 66%, and the low severity class had a producer's accuracy of only 52%. Consequently, there are misclassifications in both directions: areas that did not burn are classified as low severity, and areas that in fact burned with low severity are recorded as unburned. Nevertheless, the dNBR index seemed to have captured the fire scar and burn severity rather well in our study area with an overall accuracy of 82% and 98%. Particularly, the high severity areas can be well distinguished from the low severity burns, as the high burn severity class achieved an user's and producer's accuracy of nearly 100% for both fire years.

The reason for the misclassifications of unburned and low severity areas lies in the selection of the pre- and post-burn images. Ideally, pre- and post-burn images would be captured during the peak growing season when vegetation is green and flourishing, providing maximum contrast between unburned and burned vegetation (Key & Benson, 2006). However, in our case, we used images from September, which marks the end of the growing season when vegetation is senescent, and soil and plants are dried out (Key & Benson, 2006; Parmentier et al., 2011). Since dry vegetation imitates the impact of fire on vegetation, it becomes more difficult to distinguish burned vegetation from unburned but arid plants, making it challenging to separate the unburned class from the low severity class (Key & Benson, 2006). This is particularly the case when the post-fire image is drier than the pre-fire image (Key & Benson, 2006), which may have been the case here, as the year 2020 experienced a heatwave (Overland & Wang, 2021). Epting et al. (2005) even found a lower correlation between CBI field data and dNBR for one of the three Yukon-Charley Rivers National Preserve burns from 1999, which they attributed primarily to the September imagery. Their pre- and post-burn images used for the dNBR calculation were taken from September 12th and 16th, a time when the scrubs and woodlands, which accounted for 45% of the burned area, were already beginning to senesce (Epting et al., 2005). It is also striking that misclassifications in our burn severity map often seemed to occur around water bodies. For instance, some unburned areas near

rivers and around thermokarst lakes were mistakenly classified as low severity. This could be related to variations in the thawing of the underlying permafrost and differences in soil moisture content and water level from pre- to post-fire scene (Parmentier et al., 2011; van Huissteden et al., 2021).

The influence of the selection of pre- and post-burn images on dNBR and the challenge of finding optimal images are well-known and widely discussed (Allen & Sorbel, 2008; Chen et al., 2021a; Key & Benson, 2006; Loboda et al., 2013). In the Arctic tundra, however, this problem is exacerbated by the short growing season and the high prevalence of cloud cover (Boelman et al., 2011; Epting et al., 2005; Kolden & Rogan, 2013). In our case, the entire August 2020 was covered by clouds, which was especially strong due to the large amount of aerosols released form the fires (Figure 18 in Appendix), making it impossible to find images during peak season. Especially since the snow and ice do not start to melt until the end of Mai or beginning of June, the vegetation needs some time to react, and by the end of August or beginning of September, the vegetation is already beginning to senesce again (Parmentier et al., 2011). Other studies dealt with this problem by taking pre- and post-burn images that are further apart than the optimal 1-2 years, increasing the chance of finding cloud-free images during the peak season (Allen & Sorbel, 2008). Nonetheless, this extended time span for post-burn images could in turn negatively impact the dNBR values. This is because a few years after the occurrence of a fire, the vegetation regenerates, which diminishes the burn severity signal, leading to an underestimation of the burn (Allen & Sorbel, 2008; López García & Caselles, 1991). This is particularly the case in the tundra, which generally recovers quickly after fire (Boelman et al., 2011; Kolden & Rogan, 2013; Racine et al., 2004). The fast revegetation leads to smaller changes in dNBR values at tundra sites one year after the fire in comparison to forested plots, making it challenging to determine the fire's influence on tundra vegetation a few years after the fire (Allen & Sorbel, 2008). Kolden & Rogan (2013) made a comparison between an initial and extended assessment, whereby a decrease in severity was detected in over 40% of pixels going from initial to extended assessment. We also tested an extended assessment, as already mentioned in chapter 2.2.2, where we combined other possible pre- and post-burn images taken from June and August with intervals of 1-2 years in between, to see if the different burn severity classes can be better differentiated. However, in these combinations, the overlap of the different burn severity classes was even higher (Figure 7 and 8 in Appendix). The dNBR values of the unburned class even partially overlapped with those

of the high severity class, which is likely caused by significant changes in the unburned areas, as the images had intervals of multiple years in between and we sometimes had to use pre- and post-burn images from different months due to cloud cover (Key & Benson, 2006; Kolden & Rogan, 2013).

Ultimately, there is a trade-off between minimizing the time span between pre- and post-burn images to keep changes in vegetation not related to fire such as vegetation recovery as small as possible and having a sufficiently large time span between pre- and post-burn images to be able to find cloud-free images during peak growing season. Other studies suggest using only a single-date index, to avoid the issue of matching pre- and post-burn images, while yet others even propose the use of alternative indices such as the Relative differenced Normalized Burn Ratio, Enhanced Vegetation Index 2, or the Tasseled Cap Index, which are supposedly better at accurately mapping burn severity, although they show mixed results (Allen & Sorbel, 2008; Boelman et al., 2011; Loboda et al., 2013; Miller & Thode, 2007).

Despite the fact that our choice of pre- and post-burn images did not comply with the classic assumptions of the dNBR and other indices have been proposed for tundra wildfire research, our dNBR maps showed good performance and provide valuable information. The thresholds of the dNBR classes also fall within the range reported by other studies. For instance, they correspond roughly to the example range of dNBR thresholds reported by Key & Benson (2006) (Table 6 in Appendix). They are also comparable to the stated burn severity classes for the Anaktuvuk River fire in Alaska in 2007 (Kolden & Rogan, 2013), although these thresholds tend to be slightly higher than ours. We propose that tundra burn severity studies can use dNBR but have to account for pre- and post-burn images to be taken within the same time of the season and post-fire images to be taken before the next greening season. More field observations are needed though to improve classification and ensure correct interpretation of the burn severity maps.

The burn severity analysis showed that the northeastern Siberian tundra fires of 2019 and 2020 predominantly burned at low severity. In the Arctic tundra, there have been relatively few studies conducted on burn severity so far. There is a burn severity analysis of the Kuparuk River fire in Alaska from the year 2007, which covered an area of 725 ha of which 80% showed a low burn severity (Jones et al., 2009). This coincides with the obtained 81% and 84% low burn severity of the northeastern Siberian tundra fires from 2019 and 2020. Interestingly, the

Anaktuvuk River fire, the biggest tundra fire ever recorded on Alaska's North Slope, burned an area of 103'987 ha directly adjacent to the Kuparuk River fire in the same year, but showed 82% moderate to extreme burn severity (Jones et al., 2009). In contrast to this, the northeastern Siberian tundra fires exhibited mostly low burn severity, with only 19% and 16% of the area burning at high severity.

The discrepancy in burn severity between the geographically very close Anaktuvuk and Kuparuk River fire illustrates that extraordinary climate and weather events can result in different burn severities, emphasizing the complexity of Arctic tundra wildfires (Jones et al., 2009). The high severity of the Anaktuvuk River fire is attributed to low soil moisture content as a result of anomalously high temperatures and a precipitation deficit in the summer of 2007 (Hudspith et al., 2017; Jones et al., 2009). These drought conditions led to vegetation stress and increased susceptibility to burning (Jones et al., 2009). However, the Siberian tundra fires also experienced drought conditions, with a heatwave in 2020 (Overland & Wang, 2021) and a precipitation deficit in the summer of 2019 (van Huissteden et al., 2021), and still showed a prevalence of low severity burns. A possible explanation could be that vegetation type might be an important factor in determining burn severity in the tundra (Hudspith et al., 2017), as most of the high severity area of the Anaktuvuk River fire consisted of woody scrubs (Jones et al., 2009). The timing of the fires may have also played a role. The highest fire spread rate of the Anaktuvuk River fire occurred late in the season in September, and the fire proceeded to burn until October, while the Kuparuk River fire and Siberian tundra fires from 2019 and 2020 already stopped burning at the beginning of August and September (Jones et al., 2009). The environmental conditions occurring late in the season, such as vegetation senescence and aridity may have contributed to this high burn severity in the Anaktuvuk River fire (Jones et al., 2009). Differing fuel moisture contents over the season and between species, as well as diverse curing times are expected to lead to different burn severities (Hudspith et al., 2017). The predominance of low burn severities in the northeastern Siberian tundra fires in 2019 and 2020 thus might be a result of higher fuel moisture contents that led to less vegetation consumption (Hudspith et al., 2017)

However, a prevalence of high burn severity was expected, not only due to drought conditions, but also because the northeastern Siberian tundra fires in 2019 and 2020 had an enhanced fire intensity, as quantified by the Moderate Resolution Imaging Spectroradiometer fire

radiative power (Scholten et al., 2022). Fire intensity represents the magnitude of heat generated by a fire and is linked to burn severity, as it directly impacts the extent of wood and biomass consumption (Key & Benson, 2006). Key & Benson (2006) argue though that a high fire intensity does not necessarily correspond to a high burn severity, but that based on the composition of the vegetation, the same fire intensity can result in different burn severities. For instance, certain species may be better adapted to fire and thus remain relatively unscathed, although a high fire intensity presumably consumes even vegetation that is well adapted to fire (Key & Benson, 2006). In addition, the resulting burn severity also depends on fire residence time (Hudspith et al., 2017; Lentile et al., 2006). High intensity fires that spread rapidly may kill less vegetation because there is less heat transfer into the soil compared to low intensity fires that spread slowly (Lentile et al., 2006), which might explain why the northeastern Siberian tundra fires had both low burn severity despite high fire intensity. The overall mesic condition and fast fire propagation at tussock tundra sites, leading to reduced smouldering and thus a generally low burn severity in tundra vegetation further supports this hypothesis (Allen & Sorbel, 2008).

A low burn severity in the tundra is often associated with a combination of burned, unburned and recovered vegetation patches, where the fire consumes only a small part of the litter and vegetation, with most plants being only slightly charred and some remaining completely unburned (Hudspith et al., 2017; Jones et al., 2009; Kolden & Rogan, 2013; Loboda et al., 2013). In contrast to that, high severity burns in the Arctic tundra are generally associated with complete destruction of pre-fire vegetation and increased consumption of organic soils (Hudspith et al., 2017; Jones et al., 2009; Kolden & Rogan, 2013; Loboda et al., 2013). Moss cover and organic layers have thermal insulation properties, and a reduction of these layers as a result of high burn severity therefore leads to warmer soils and deeper thaw depths (Rocha et al., 2012; Rocha & Shaver, 2011b). In a study by Rocha & Shaver (2011a), the soil temperature at high burn severity sites was 53% higher than at unburned locations. At moderate burn severity sites, the soil temperature was still 42% higher compared to unburned ones (Rocha & Shaver, 2011a). This is particularly of concern because increased soil temperatures can result in increased decomposition of soil carbon, permafrost degradation and formation of thermokarst, causing higher carbon emissions (Rocha et al., 2012). On the Seward Peninsula in Alaska for instance, the thickness of the permafrost active layer returned

to the original pre-burn state at low burn severity sites, at high severity locations, however, the permafrost was thawed considerably (Racine et al., 2004).

Since burn severity affects both the destruction and regeneration of vegetation, tundra fires can also induce changes in the net ecosystem exchange of CO_2. In the Anaktuvuk River fire, the cumulative net ecosystem exchange was 154 g C/m^2 higher at high burn severity sites and 82 g C/m^2 higher at moderate burns compared to unburned locations at the end of the summer one year post-fire. This implies that high severity burns absorb less CO_2 than moderate or completely unburned spots, demonstrating how important it is to consider burn severity when it comes to post-fire carbon emissions. Furthermore, it illustrates that Arctic fire management could be relevant to mitigate the severity and dimension of fires to prevent large CO_2 emissions (Rocha & Shaver, 2011a).

Tundra fires in Alaksa have also been observed to lead to changes in vegetation composition (Racine et al., 2004). On the Seward Peninsula for instance, post-fire shrub cover was larger, while mosses and lichens showed only slight to no regeneration at all even 24 years after the fire (Racine et al., 2004). Hudspith et al. (2017) even found that fires with a low to moderate burn severity can change the composition of vegetation in the short-term, as shrub-tussock had transformed into tussock tundra one year after the fire.

Tundra fires therefore have varying environmental consequences depending on the burn severity of a fire, including vegetation succession, permafrost degradation as well as increased soil temperatures and carbon emissions (Racine et al., 2004; Rocha et al., 2012; Rocha & Shaver, 2011a; Rocha & Shaver 2011b). As the majority of the area of the northeastern Siberian tundra fires in 2019 and 2020 have burned with low burn severity (roughly 80% of the total area) we expect the ecological impact to be rather minimal. However, the high severity burns should not be underestimated in terms of their impact on permafrost, carbon emissions and vegetation, because even though only about 20% of the area burned with high severity, this is still equivalent to an area of 24 km^2 and 106 km^2. Ideally, the burn severity analysis using remote sensing would have been complemented by in-situ field sampling, where a Composite Burn Index is determined (Key & Benson, 2006). The CBI is a sampling strategy that ecologically assesses burn severity and measures soil effects directly in the field, in a manner that allows for the field characteristics to be captured by remote sensing (Key & Benson, 1999). This way, the burn severity recorded by remote sensing (dNBR) can be directly correlated with fire

effects measured in the field (Key & Benson, 1999). However, within the scope of this study and due to current geopolitical reasons, it was not feasible for us to conduct in-situ measurements of burn severity in the Russian tundra. Thus, the ecological impact of the burn severities determined using satellite data can only be inferred from other studies conducted in the tundra. Nevertheless, as several studies in the Arctic tundra have already demonstrated a strong correlation between dNBR and CBI (with R^2 values around 0.8) (Allen & Sorbel, 2008; Jones et al., 2009; Kolden & Rogan, 2013), we assume that the burn severities determined by remote sensing in this study also effectively captured the actual fire effects in the field and will be similar to already existing surveys.

Combining the low and high burn severity areas, the 2019 and 2020 tundra fires covered an area of about 125 km^2 and 645 km^2 respectively. Compared to the mean burned area per year in the Russian tundra from 1996 to 2002, which amounts to 2'079 km^2 per year (Sukhinin et al., 2004), the fires account for 6% and 31% respectively. According to the fire size classification described by Talucci et al. (2022), the 2019 fire falls into the category of large fires (10'000 < 50'000 ha), while the 2020 fire even belongs to the extremely large fire class (50'000 < 100'000 ha). This demonstrates how large the extent of these fires was. Although they predominantly burned with low severity, the ecological impact that these fires might had should not be overlooked. More in-situ data of burn severity is necessary though for a better understanding of the consequences of the Siberian tundra fires. As burn severity maps serve as the foundation for a wide range of further research, this also offers the opportunity to investigate in subsequent analyses how these different burn severities detected in the northeastern Siberian tundra fires affected soil temperature, permafrost, vegetation succession and carbon emissions. It is crucial that short-term and long-term consequences of differing burn severities in the Siberian tundra are assessed, in particular because most studies on burn severity have been performed in Alaska (Rocha & Shaver, 2011a; Rocha & Shaver 2011b).

4.2 Variation of the high severity burns within and between the fire scars

The high severity patch size analysis revealed that within the fire scars, there are more small high severity patches than large ones. Different patch sizes suggest that varying environmental conditions may have prevailed across the burns (Boelman et al., 2011). Burn severity depends on numerous factors, including fire weather, fuel availability, fuel abundance, fuel moisture, soil moisture, fire intensity, topography, and climate (Chen et al., 2020b; Hudspith et al., 2017;

Jones et al., 2009; Key & Benson, 2006; Parks et al., 2018; Racine et al., 2004). Depending on the interaction of these variables, different burn patterns can evolve, from a homogeneous area to a mosaic of patches with varying burn severity (Boelman et al., 2011).

The fact that the 2019 and 2020 fire had a similar patch size distribution (with many more small high severity patches than large ones) is likely due to similar environmental conditions, as the two fires are directly adjacent and correspondingly have similar vegetation and topography. A higher percentage of the area that burned at high severity and larger high severity burns were expected in 2020 though, as there was a heatwave this year (Overland & Wang, 2021). However, the year 2019 was also very warm and dry, accompanied by a precipitation deficit in summer (van Huissteden et al., 2021), suggesting that both years had similar meteorological conditions.

The 2020 fire had a greater mean patch size in comparison to the 2019 fire and exhibited a larger maximum patch size with an area of about 2 km^2. This might be attributable to the size of the fire, with the 2020 fire being almost five times as large as the 2019 fire. A study by Buonanduci et al. (2023), which examined 1'615 fires distributed across the entire Northwest of the United States, was able to demonstrate that with increasing fire size, larger high severity patches occur. Larger fires, burning over an extended period of time, are exposed to a wider spectrum of meteorological conditions (Buonanduci et al., 2023). Due to their size, they also encompass a broader range of vegetation and topographical characteristics (Buonanduci et al., 2023). This diverse array of conditions, together with temporally and spatially changing top-down and bottom-up controls, lead to the emergence of varying patch sizes, which comprise numerous small patches as well as a few large ones (Buonanduci et al., 2023). In comparison to the patch sizes reported by Buonanduci et al. (2023), where the area-weighted means of some fire regimes reached values from over 100 to 10'000 hectares, the maximum patch sizes from the 2019 fire and 2020 fires were relatively small.

The patch size analysis has shown that the smallest high severity patch size has an area of 400 m^2, which corresponds exactly to the size of a pixel. This abundance of single-pixel patches might be the result of setting the threshold separating the low and high burn severity class, too low (Key & Benson, 2006). Buonanduci et al. (2023) applied a smoothing filter in their high severity patch analysis to remove such single-pixel patches in order to decrease their impact on the analysis. On the other hand, these single-pixel patches might demonstrate that the

northeastern Siberian tundra fires have a small-scale burn severity pattern. The Anaktuvuk River fire for instance generated a mosaic of patches ranging from small (1 m^2) to large (> 100m^2) (Boelman et al., 2011). This suggests that the spatial resolution of 20 m used here, although higher than the commonly used 30 m of Landsat thematic mapper sensor spatial resolution of other burn severity studies in the Arctic (Allen & Sorbel, 2008; Jones et al., 2009), may still be too small to capture the spatial pattern of burn severity in the tundra, as any fine-scale spatial patterns of burn severity (< 20 m) will not be captured. A study from Boelman et al. (2011) compared burn severity maps from Quickbird (2.4 m Pixel) to Landsat thematic mapper (30 m Pixel) showing that the number of pixels per burn severity class was similar between both maps. However, they also highlighted that in the Landsat image, there were regions that were classified as intermediate burn severity, while the Quickbird sensor was able to identify it as a high severity patch next to a small unburned area (Boelman et al., 2011). Therefore, the use of a higher resolution remote sensing imagery might be useful to provide a higher accuracy of the spatial variability of the different burn severities in our study area, which would offer increased reliability for subsequent analyses, depending on the research question posed (Allen & Sorbel, 2008). A spatial resolution of 20 m is probably high enough for capturing large-scale effects, such as carbon emissions, erosion-prone areas or wide-scale shifts in vegetation (Allen & Sorbel, 2008). For small-scale effects, such as local permafrost changes and vegetation recovery, however, the resolution might be too small (Allen & Sorbel, 2008). Especially since soil moisture and vegetation can vary greatly over short distances in the Arctic tundra (Lara et al., 2018).

Nevertheless, high severity patches are of great ecological importance. As already discussed in chapter 4.1, high severity sites can lead to changes in vegetation, permafrost degradation and increased carbon emissions (Racine et al., 2004; Rocha et al., 2012; Rocha & Shaver, 2011a). However, the patch size of the high severity areas also plays an important role. In forest ecosystems for instance, large high severity patches can reduce the resilience of forests, because the inside of large patches is further away from the seed source and thus tends to recover at a slower rate (Buonanduci et al., 2023; Coop et al., 2020). As a result, there is a risk that high severity forest patches will transform into non-forest vegetation (Buonanduci et al., 2023; Coop et al., 2020). A similar process was observed in the Alaskan tundra. A study showed that in places where the burn severity was high and thus a large part of the organic soil was consumed, the underlying mineral soils were exposed where the seeds of willow shrubs were

able to sprout, thereby promoting their spread (Racine et al., 2004). As a consequence, high severity tundra fires pose a risk for seed germination of trees and shrubs through mineral soil exposure, driving vegetation shifts such as the expansion of the treeline and shrub dispersion (Racine et al., 2004). It is therefore crucial that not only the percentage of high severity area is considered, but also the different patch sizes, as these can have important implications for vegetation succession.

The patch size analysis of the high severity burns showed high variation in patch areas, using medium-resolution imagery in two fire scars only. Our method could therefore be applied to further fire scars to test if that pattern of many small and a few large patches holds across the Arctic tundra.

4.3 Burn severity relation to vegetation type

In our study area, elevation and TPI served as a proxy for the vegetation type. The linear regression revealed a significant positive relationship (p-value < 0.01) between dNBR and elevation, indicating that there is a slight tendency that with higher elevation, burn severity is more severe. However, the scattering was very large, demonstrating that a wide range of dNBR values can occur, irrespective of elevation. An explanation for this large scatter could be that the Yedoma ridges, where we expected higher burn severity, do not all lie at the same elevation. If one Yedoma ridge has an elevation of 20 m while another has a height of 40 m, then this partly explains the dispersion of the dNBR values and why we also find high burn severity at lower elevations. For this reason, TPI was tested in addition to elevation, which should better represent the topographic features of the study area such as low-lying drained thaw lake basins and Yedoma ridges. However, despite a significant positive relationship between dNBR and TPI (p-value < 0.01), the scattering was still very large. Consequently, in our study area, both TPI and elevation and thus vegetation seem not to be good predictors of burn severity. Our results suggest that lower elevations and basins covered by sedges (Khitun et al., 2020; Parmentier et al., 2011; van Huissteden et al., 2021) can burn just as severely as the tussock-tundra dominated higher elevations (Khitun et al., 2020; van Huissteden et al., 2021), and that Yedoma ridges do not necessarily coincide with a high burn severity.

The R^2 from the linear regressions were very low (R^2 = 0.1751 (2019) and R^2 = 0.1741 (2020)), indicating that there might be other variables that are more important than elevation and TPI, i.e. vegetation, for predicting burn severity. Therefore, we also tested the relationship between

dNBR and aspect, as well as dNBR and slope (Figure 17 in Appendix), as these two variables were relevant for burn severity in other studies outside the tundra (Birch et al., 2015; Dillon et al., 2011). However, no significant linear relationship between dNBR and aspect was observed in our study area. Regardless of the direction that a slope faced, both high and low burn severities occurred. Concerning the slope, the high dNBR values seemed to visually cluster around 5°, while above and below this threshold, the dNBR values tended to decrease again. But also in this case, the scattering was very large and due to heteroscedasticity, we applied no linear model that could test for the significance of this visual relationship.

In contrast to our findings, other studies show that burn severity differs depending on vegetation type (Allen & Sorbel, 2008; Epting et al., 2005). For instance, needleleaf forests are generally more combustible compared to broadleaf forests (Epting et al., 2005), and black and white spruce exhibit a higher burn severity than deciduous trees and tundra vegetation (Allen & Sorbel, 2008). However, burn severity can also vary within the same vegetation type. While tussock tundra and low-shrub tussock tundra showed low burn severity in the study from Allen & Sorbel (2008), there were also high burn severity areas which comprised of completely consumed tussock cottongrass (*Eriophorum vaginatum L.*). Furthermore, Arctic tundra wildfires seem to favour certain types of vegetation (Rocha et al., 2012). Moist and wet tussocks as well as moist shrubs burn more often than one would expect due to their surface coverage, in contrast to moist non-acidic and barren tundra, that seem to burn less frequently (Rocha et al., 2012). For instance, barrens make up 5% of the Alaskan tundra but account for only 1% of the area burned, while moist tussock tundra makes up 41% of the ecoregion, but accounts for 47% of the burned area, which is presumably linked to fuel loads and differences in aboveground biomass (Rocha et al., 2012).

Chen et al. (2020b) analysed Alaskan tundra fires and found that high burn severities predominantly occurred in drier upland areas. Dry areas showed moderate to high burn severities, while depressions that were water-saturated did not burn at all (Chen et al., 2020b). The burn severity progressively increased moving from low-lying areas dominated by wet graminoids to arid dwarf-shrub dominated highlands (Chen et al., 2020b). Similarly, Racine et al. (2004) observed in their study area in the Arctic tundra of Alaska at Nimrod Hill in the Seward Peninsula, that burn severity correlates with slope and drainage. They found that the poorly drained moist-tussock shrub tundra on the foot slope burned less severely compared

to the dwarf shrub tundra on the well-drained, steep slope, where vegetation and organic soil consumption was much higher (Racine et al., 2004). On the poorly drained flat crest, on the other hand, which harbours wet sedge meadows, burn severity was low again (Racine et al., 2004). A similar pattern was expected in our study area in the Kytalyk region, where the well-drained Yedoma ridges might be dry due to drainage and flow patterns and correspondingly burned at higher burn severity. Although we found a significant positive linear relationship between dNBR and TPI respectively elevation, the spatial pattern of burn severity is not as clear-cut as in the study from Chen et al. (2020b) or Racine et al. (2004), since high burn severity occurred both on Yedoma ridges and in low-lying drained thaw lake basins.

Thus, the burn severity in our study area cannot be fully explained by vegetation type, as indicated by the low R^2 values and the large scatter in the relationships between dNBR and elevation and TPI. Topography, respectively vegetation, certainly had an influence (see positive, significant relationship), but there are many other factors which were probably even more important in relation to burn severity. Burn severity is a complex phenomenon, with many different variables impacting the resulting severity of a fire. We suppose that other variables such fire residence time (Hudspith et al., 2017; Lentile et al., 2006), fire weather (Jones et al., 2009) and fuel and soil moisture (Hudspith et al., 2017; Jones et al., 2009) have influenced how severely a site has burned in the northeastern Siberian tundra fires. Although some of these factors might indirectly already be accounted for in topography and vegetation type, using such factors directly instead of a proxy might result in better predictions of burn severities (Dillon et al., 2011).

In another study, concerning western United States forests, fire weather has been recognized as a very important factor affecting burn severity, with the potential to reduce high severity fires (Parks et al., 2018). In boreal forests, wind speed, relative humidity and the time period since last precipitation were found to be the most important factors influencing high severity patch sizes (Wu et al., 2018). With decreasing relative humidity (drier conditions), the patch size increased, while with stronger winds, the patches were more clustered (Wu et al., 2018). Meteorological variables also play a major role in tundra fires, where the moisture content and susceptibility of fuels to burn is mostly controlled by weather and climate (Jones et al., 2009). We therefore assume that not only bottom-up factors such as vegetation and topography but also top-down effects such as fire weather influenced the different burn severities detected

within the fire scars in our study area. This is consistent with the analysis of patch sizes of northwestern United States fires from Buonanduci et al. (2023), which suggests that the spatial variability of burn severity of fires of small to moderate size (meaning 400 – 10'000 ha) is primarily determined by either top-down or bottom-up factors, while for large fires both top-down and bottom-up factors are important. As the 2019 and the 2020 fire cover an area larger than 10'000 ha, this would indicate that not only bottom-up factors such as vegetation were important for the burn severity, but also top-down factors such as fire weather. Under extreme weather and climate conditions, such as extraordinary dry years, which was the case for both the 2019 and 2020 fire (Overland & Wang, 2021; van Huissteden et al., 2021), bottom-up factors such as topography were found to have little influence on fire behaviour and were overpowered by top-down controls, while under non-extreme meteorological conditions, topographical variables showed a larger impact (Dillon et al., 2011; Turner & Romme, 1994). However, if this hypothesis holds true for the northeastern Siberian tundra fires would need to be confirmed in further analyses.

It is also worth mentioning that there might be some uncertainty regarding the proxies. Due to the lack of sufficiently high-resolved vegetation maps and field observations in our study area, we could not test for a linkage between vegetation type and proxies. Still, we approximated vegetation with topography (elevation and TPI) because several studies suggest that vegetation is linked to topography in this region (Khitun et al., 2020; Loranty et al., 2014; Parmentier et al., 2011; van Huissteden et al., 2021). Vegetation (Chen et al., 2020b; Racine et al., 2004), fuel moisture (Hudspith et al., 2017), soil moisture (Hudspith et al., 2017; Jones et al., 2009), fire weather (Jones et al., 2009; Parks et al., 2018), residence time (Hudspith et al., 2017; Lentile et al., 2006) and other factors are important for shaping burn severity in the Arctic tundra. Thus, more variables should be included in further analyses, in particular also top-down factors, to better understand and predict the occurrence of low and high burn severities.

5 Conclusion

In Siberia, major fires occurred in the years 2019 and 2020, with exceptionally large burned areas far north extending into the tundra. Our results have shown that these northeastern Siberian tundra fires from 2019 and 2020 burned predominantly with low burn severity, which is typical for Arctic tundra fires under mesic conditions. The low burn severity class accounted for 81% and 84% of the 2019 respectively 2020 fire scar, and only 19% and 16% of the area burned with high severity. The high burn severity area of each fire consisted of a mosaic of many small and a few large burn patches, suggesting that different environmental conditions prevailed across the burned area. As fires have different ecological impacts depending on the burn severity, these findings emphasize the importance of considering the spatial pattern of tundra fires and their varying burn severity in models attempting to simulate post-fire carbon emissions, permafrost degradation or vegetation succession. However, more in-situ burn severity data are necessary to validate and calibrate the burn severity maps.

The dNBR values showed a significant positive linear relationship (p-value < 0.01) with elevation and TPI, which served as proxies for vegetation types in our study. However, the dispersion was very large, and both low and high burn severity values occurred in drained thaw lake beds as well as on Yedoma ridges. Therefore, vegetation could not fully explain the distribution of the dNBR values in our study area, as indicated by the low R^2 values (R^2 = 0.1751 and R^2 = 0.1741). Additionally, burn severity did not have a significant relationship with other topographic variables such as aspect, suggesting that the different burn severities of the northeastern Siberian tundra fires in 2019 and 2020 might have been less influenced by bottom-up effects such as vegetation and topography and more by other factors like fire residence time and top-down controls such as fire weather and wind. Further analysis confirming this would be necessary though.

The generated burn severity maps serve as a basis for further research on tundra fires. In subsequent analyses, it would be important to investigate how the different burn severities have affected permafrost degradation, vegetation succession and carbon emissions, to better understand the ecological and climatological consequences of the Siberian tundra fires. Studies predict that Arctic tundra fires will occur more frequently in the future due to global warming and Arctic amplification. Therefore, it is crucial that further research is conducted to better understand the occurrence and burn severities of fires, so that any necessary fire

management measures could be implemented. In particular because changes in the Arctic fire regime could potentially lead to a significant carbon release, due to their large soil carbon storage, further contributing to climate warming. Further research should be encouraged especially in the Siberian Arctic tundra, where there is a lack of studies on burn severity.

6 Acknowledgement

I would like to take this opportunity to thank all those who have supported and motivated me during this thesis. First and foremost, I would like to thank my daily supervisor Nils Rietze for his support and help. Thank you very much for the tips, inputs, and suggestions for my analysis, as well as your detailed feedback on the thesis and the visualization of the maps and graphics. Many thanks also for always taking your time. I would also like to thank Prof. Dr. Gabriela Schaepman-Strub for her valuable insights and feedback throughout the entire process of my master's thesis. Special thanks also go to Dr. Jakob Assmann for his helpful tips for the burn severity classification. Finally, I want to thank my family and my friends for their continuous encouragement throughout the whole process of this master's thesis. This work would not have been possible without you. Thank you all very much.

7 References

Alcaras, E., Costantino, D., Guastaferro, F., Parente, C., & Pepe, M. (2022). Normalized Burn Ratio Plus (NBR+): A New Index for Sentinel-2 Imagery. *Remote Sensing*, *14*(7), 1–19. https://doi.org/10.3390/rs14071727

Allen, J. L., & Sorbel, B. (2008). Assessing the differenced Normalized Burn Ratio's ability to map burn severity in the boreal forest and tundra ecosystems of Alaska's national parks. *International Journal of Wildland Fire*, *17*(4), 463–475. https://doi.org/10.1071/WF08034

Birch, D. S., Morgan, P., Kolden, C. A., Abatzoglou, J. T., Dillon, G. K., Hudak, A. T., & Smith, A. M. S. (2015). Vegetation, topography and daily weather influenced burn severity in central Idaho and western Montana forests. *Ecosphere*, *6*(1). https://doi.org/10.1890/ES14-00213.1

Blok, D., Heijmans, M. M. P. D., Schaepman-Strub, G., van Ruijven, J., Parmentier, F. J. W., Maximov, T. C., & Berendse, F. (2011). The Cooling Capacity of Mosses: Controls on Water and Energy Fluxes in a Siberian Tundra Site. *Ecosystems*, *14*(7), 1055–1065. https://doi.org/10.1007/s10021-011-9463-5

Boelman, N. T., Rocha, A. V., & Shaver, G. R. (2011). Understanding burn severity sensing in arctic tundra: Exploring vegetation indices, suboptimal assessment timing and the impact of increasing pixel size. *International Journal of Remote Sensing*, *32*(22), 7033–7056. https://doi.org/10.1080/01431161.2011.611187

Buonanduci, M. S., Donato, D. C., Halofsky, J. S., Kennedy, M. C., & Harvey, B. J. (2023). Consistent spatial scaling of high-severity wildfire can inform expected future patterns of burn severity. *Ecology Letters*, *26*(10), 1687–1699. https://doi.org/10.1111/ele.14282

Chen, D., Fu, C., Hall, J. V., Hoy, E. E., & Loboda, T. V. (2021a). Spatio-temporal patterns of optimal Landsat data for burn severity index calculations: Implications for high northern latitudes wildfire research. *Remote Sensing of Environment*, *258*. https://doi.org/10.1016/j.rse.2021.112393

Chen, D., Loboda, T. V., & Hall, J. V. (2020a). A systematic evaluation of influence of image selection process on remote sensing-based burn severity indices in North American boreal forest and tundra ecosystems. *ISPRS Journal of Photogrammetry and Remote Sensing*, *159*, 63–77. https://doi.org/10.1016/j.isprsjprs.2019.11.011

Chen, Y., Lara, M. J., & Hu, F. S. (2020b). A robust visible near-infrared index for fire severity mapping in Arctic tundra ecosystems. *ISPRS Journal of Photogrammetry and Remote Sensing*, *159*, 101–113. https://doi.org/10.1016/j.isprsjprs.2019.11.012

Chen, Y., Romps, D. M., Seeley, J. T., Veraverbeke, S., Riley, W. J., Mekonnen, Z. A., & Randerson, J. T. (2021b). Future increases in Arctic lightning and fire risk for permafrost carbon. *Nature Climate Change*, *11*(5), 404–410. https://doi.org/10.1038/s41558-021-01011-y

Coop, J. D., Parks, S. A., Stevens-Rumann, C. S., Crausbay, S. D., Higuera, P. E., Hurteau, M. D., Tepley, A., Whitman, E., Assal, T., Collins, B. M., Davis, K. T., Dobrowski, S., Falk, D. A., Fornwalt, P. J., Fulé, P. Z., Harvey, B. J., Kane, V. R., Littlefield, C. E., Margolis, E. Q., … Rodman, K. C. (2020). Wildfire-Driven Forest Conversion in Western North American Landscapes. *BioScience*, *70*(8), 659–673. https://doi.org/10.1093/biosci/biaa061

Descals, A., A Gaveau, D. L., Verger, A., Sheil, D., Naito, D., & Peñuelas, J. (2022). Unprecedented fire activity above the Arctic Circle linked to rising temperatures. *Science*, *378*(6619), 532–537. https://doi.org/DOI: 10.1126/science.abn9768

Dillon, G. K., Holden, Z. A., Morgan, P., Crimmins, M. A., Heyerdahl, E. K., & Luce, C. H. (2011). Both topography and climate affected forest and woodland burn severity in two regions of the western US, 1984 to 2006. *Ecosphere*, *2*(12). https://doi.org/10.1890/ES11-00271.1

Epting, J., Verbyla, D., & Sorbel, B. (2005). Evaluation of remotely sensed indices for assessing burn severity in interior Alaska using Landsat TM and ETM+. *Remote Sensing of Environment*, *96*(3–4), 328–339. https://doi.org/10.1016/j.rse.2005.03.002

ESA (2023). Sentinel-2 MSI User Guide. https://sentinel.esa.int/web/sentinel/user-guides/sentinel-2-msi. Accessed: 05.10.2023

Flannigan, M., Cantin, A. S., De Groot, W. J., Wotton, M., Newbery, A., & Gowman, L. M. (2013). Global wildland fire season severity in the 21st century. *Forest Ecology and Management*, *294*, 54–61. https://doi.org/10.1016/j.foreco.2012.10.022

Flannigan, M. D., Wotton, B. M., Marshall, G. A., de Groot, W. J., Johnston, J., Jurko, N., & Cantin, A. S. (2016). Fuel moisture sensitivity to temperature and precipitation: climate change implications. *Climatic Change*, *134*(1–2), 59–71. https://doi.org/10.1007/s10584-015-1521-0

Fung, T., & Ledrew, E. (1988). The Determination of Optimal Threshold Levels for Change Detection Using Various Accuracy Indices. *Photogrammetric Engineering and Remote Sensing*, *54*(10), 1449–1454.

GEE (2023). Google Earth Engine. https://earthengine.google.com/. Accessed: 04.10.2023

Hesselbarth, M. H. K., Sciaini, M., With, K. A., Wiegand, K., & Nowosad, J. (2019). landscapemetrics: an open-source R tool to calculate landscape metrics. *Ecography*, *42*(10), 1648–1657. https://doi.org/10.1111/ecog.04617

Holloway, J. E., Lewkowicz, A. G., Douglas, T. A., Li, X., Turetsky, M. R., Baltzer, J. L., & Jin, H. (2020). Impact of wildfire on permafrost landscapes: A review of recent advances and future prospects. *Permafrost and Periglacial Processes*, *31*(3), 371–382. https://doi.org/10.1002/ppp.2048

Hudspith, V. A., Belcher, C. M., Barnes, J., Dash, C. B., Kelly, R., & Hu, F. S. (2017). Charcoal reflectance suggests heating duration and fuel moisture affected burn severity in four Alaskan tundra wildfires. *International Journal of Wildland Fire*, *26*(4), 306–316. https://doi.org/10.1071/WF16177

Jones, B., Kolden, C., Jandt, R., Abatzoglou, J., Urban, F., & Arp, C. (2009). Fire behavior, weather, and burn severity of the 2007 anaktuvuk river tundra fire, North Slope, Alaska. *Arctic, Antarctic, and Alpine Research*, *41*(3), 309–316. https://doi.org/10.1657/1938-4246-41.3.309

Key, C. H., & Benson, N. C. (1999). Measuring and remote sensing of burn severity: the CBI and NBR. *Joint Fire Science Conference and Workshop*. http://jfsp.nifc.gov/conferenceproc/index.htm

Key, C. H., & Benson, N. C. (2006). Landscape Assessment: Ground measure of severity, the Composite Burn Index; and Remote sensing of severity, the Normalized Burn Ratio. In D. C. Lutes, R. E. Keane, J. F. Caratti, C. H. Key, N. C. Benson, S. Sutherland, & L. J. Gangi (Eds.), *FIREMON: Fire Effects Monitoring and Inventory System* (RMRS-GTR-164, pp. 1–51). USDA Forest Service. https://www.researchgate.net/publication/241687027

Khitun, O. V., Koroleva, T. T., Petrovsky, V. V., Iturrate-Garcia, M., & Schaepman-Strub, G. (2020). Study of the vascular plants diversity in the surroundings of the Kytalyk Research Station (Arctic Yakutia). *III Russian National Conference "Information Technology in Biodiversity Research," 1*, 37–50. https://doi.org/10.3897/ap.2.e57091

Kolden, C. A., & Rogan, J. (2013). Mapping Wildfire Burn Severity in the Arctic Tundra from Downsampled MODIS Data. *Arctic, Antarctic, and Alpine Research*, *45*(1), 64–76. https://doi.org/10.1657/1938-4246-45.l.64

Lara, M. J., Nitze, I., Grosse, G., & McGuire, A. D. (2018). Data descriptor: Tundra landform and vegetation productivity trend maps for the arctic coastal plain of Northern Alaska. *Scientific Data*, *5*(180058). https://doi.org/10.1038/sdata.2018.58

Lentile, L. B., Holden, Z. A., Smith, A. M. S., Falkowski, M. J., Hudak, A. T., Morgan, P., Lewis, S. A., Gessler, P. E., & Benson, N. C. (2006). Remote sensing techniques to assess active fire characteristics and post-fire effects. *International Journal of Wildland Fire*, *15*(3), 319–345. https://doi.org/10.1071/WF05097

Liu, P., Liu, Y., Guo, X., Zhao, W., Wu, H., & Xu, W. (2023). Burned area detection and mapping using time series Sentinel-2 multispectral images. *Remote Sensing of Environment*, *296*. https://doi.org/10.1016/j.rse.2023.113753

Llorens, R., Sobrino, J. A., Fernández, C., Fernández-Alonso, J. M., & Vega, J. A. (2021). A methodology to estimate forest fires burned areas and burn severity degrees using Sentinel-2 data. Application to the October 2017 fires in the Iberian Peninsula. *International Journal of Applied Earth Observation and Geoinformation*, *95*. https://doi.org/10.1016/j.jag.2020.102243

Loboda, T. V., French, N. H. F., Hight-Harf, C., Jenkins, L., & Miller, M. E. (2013). Mapping fire extent and burn severity in Alaskan tussock tundra: An analysis of the spectral response of tundra vegetation to wildland fire. *Remote Sensing of Environment*, *134*, 194–209. https://doi.org/10.1016/j.rse.2013.03.003

López García, M. J., & Caselles, V. (1991). Mapping burns and natural reforestation using thematic mapper data. *Geocarto International*, *6*(1), 31–37. https://doi.org/10.1080/10106049109354290

Loranty, M. M., Natali, S. M., Berner, L. T., Goetz, S. J., Holmes, R. M., Davydov, S. P., Zimov, N. S., & Zimov, S. A. (2014). Siberian tundra ecosystem vegetation and carbon stocks four decades after wildfire. *Journal of Geophysical Research: Biogeosciences*, *119*(11), 2144–2154. https://doi.org/10.1002/2014JG002730

Mack, M. C., Bret-Harte, M. S., Hollingsworth, T. N., Jandt, R. R., Schuur, E. A. G., Shaver, G. R., & Verbyla, D. L. (2011). Carbon loss from an unprecedented Arctic tundra wildfire. *Nature*, *475*(7357), 489–492. https://doi.org/10.1038/nature10283

McCarty, J. L., Aalto, J., Paunu, V. V., Arnold, S. R., Eckhardt, S., Klimont, Z., Fain, J. J., Evangeliou, N., Venäläinen, A., Tchebakova, N. M., Parfenova, E. I., Kupiainen, K., Soja, A. J., Huang, L., & Wilson, S. (2021). Reviews and syntheses: Arctic fire regimes and emissions in the 21st century. *Biogeosciences*, *18*(18), 5053–5083. https://doi.org/10.5194/bg-18-5053-2021

McFeeters, S. K. (1996). The use of the Normalized Difference Water Index (NDWI) in the delineation of open water features. *International Journal of Remote Sensing*, *17*(7), 1425–1432. https://doi.org/10.1080/01431169608948714

McKnight, P., & Najab, J. (2010). Mann-Whitney U Test. In I. B. Weiner & W. E. Craighead (Eds.), *The Corsini Encyclopedia of Psychology*. John Wiley & Sons Inc. https://doi.org/https://doi.org/10.1002/9780470479216.corpsy0524

Miller, J. D., & Thode, A. E. (2007). Quantifying burn severity in a heterogeneous landscape with a relative version of the delta Normalized Burn Ratio (dNBR). *Remote Sensing of Environment*, *109*(1), 66–80. https://doi.org/10.1016/j.rse.2006.12.006

Natali, S. M., Holdren, J. P., Rogers, B. M., Treharne, R., Duffy, P. B., Pomerance, R., & MacDonald, E. (2021). Permafrost carbon feedbacks threaten global climate goals. *Proceedings of the National Academy of Sciences of the United States of America*, *118*(21). https://doi.org/10.1073/pnas.2100163118

Overland, J. E., & Wang, M. (2021). The 2020 Siberian heat wave. *International Journal of Climatology*, *41*(S1), E2341–E2346. https://doi.org/10.1002/joc.6850

Parks, S. A., Holsinger, L. M., Panunto, M. H., Jolly, W. M., Dobrowski, S. Z., & Dillon, G. K. (2018). High-severity fire: Evaluating its key drivers and mapping its probability across western US forests. *Environmental Research Letters*, *13*(4). https://doi.org/10.1088/1748-9326/aab791

Parmentier, F. J. W., Van Der Molen, M. K., Van Huissteden, J., Karsanaev, S. A., Kononov, A. V., Suzdalov, D. A., Maximov, T. C., & Dolman, A. J. (2011). Longer growing seasons do not increase net carbon uptake in the northeastern Siberian tundra. *Journal of Geophysical Research: Biogeosciences*, *116*(4), 1–11. https://doi.org/10.1029/2011JG001653

Porter, C., Morin, P., Howat, I., Noh, M., Bates, B., Peterman, K., Kenneth, K., Keesey, S., Schlenk, M., Gardiner, J., Tomko, K., Willis, M., Kelleher, C., Cloutier, M., Husby, E., Foga, S., Nakamura, H., Platson, M., Wethington, M. Jr., Williamson, C., Bauer, G., Enos, J., Arnold, G., Kramer, W., Becker, P., Doshi, A., D'Souza, C., Cummens, P., Laurier, F., Bojesen, M. (2018). Arctic DEM. Version 3. Harvard Dataverse V1. https://doi.org/10.7910/DVN/OHHUKH

Post, W. M., Emanuel, W. R., Zinke, P. J., & Stangenberger, A. G. (1982). Soil carbon pools and world life zones. *Nature*, *298*(8), 156–159. https://doi.org/https://doi.org/10.1038/298156a0

Racine, C., Jandt, R., Meyers, C., & Dennis, J. (2004). Tundra fire and vegetation change along a hillslope on the Seward Peninsula, Alaska, U.S.A. *Arctic, Antarctic, and Alpine Research*, *36*(1), 1–10. https://doi.org/10.1657/1523-0430(2004)036[0001:TFAVCA]2.0.CO;2

Rantanen, M., Karpechko, A. Y., Lipponen, A., Nordling, K., Hyvärinen, O., Ruosteenoja, K., Vihma, T., & Laaksonen, A. (2022). The Arctic has warmed nearly four times faster than the globe since 1979. *Communications Earth and Environment*, *3*(1). https://doi.org/10.1038/s43247-022-00498-3

Rocha, A. V., Loranty, M. M., Higuera, P. E., MacK, M. C., Hu, F. S., Jones, B. M., Breen, A. L., Rastetter, E. B., Goetz, S. J., & Shaver, G. R. (2012). The footprint of Alaskan tundra fires during the past half-century: Implications for surface properties and radiative forcing. *Environmental Research Letters*, *7*(4). https://doi.org/10.1088/1748-9326/7/4/044039

Rocha, A. V., & Shaver, G. R. (2011a). Burn severity influences postfire CO2 exchange in arctic tundra. *Ecological Applications*, *21*(2), 477–489. https://doi.org/10.1890/10-0255.1

Rocha, A. V., & Shaver, G. R. (2011b). Postfire energy exchange in arctic tundra: The importance and climatic implications of burn severity. *Global Change Biology*, *17*(9), 2831–2841. https://doi.org/10.1111/j.1365-2486.2011.02441.x

Schirrmeister, L., Froese, D., Tumskoy, V., Grosse, G., & Wetterich, S. (2013). Yedoma: Late Pleistocene Ice-Rich Syngenetic Permafrost of Beringia. In S. A. Elias (Ed.), *The Encyclopedia of Quaternary Science* (Vol. 3, pp. 542–552). Elsevier. https://doi.org/DOI:10.1016/b978-0-444-53643-3.00106-0

Scholten, R. C., Luo, F., & Veraverbeke, S. (2022). Early snowmelt and polar jet dynamics co-influence recent extreme Siberian fire seasons. *Science*, *378*, 1005–1009. https://doi.org/DOI:10.1126/science.abn4419

Serreze, M. C., & Francis, J. A. (2006). The arctic amplification debate. *Climatic Change*, *76*(3–4), 241–264. https://doi.org/10.1007/s10584-005-9017-y

Sukhinin, A. I., French, N. H. F., Kasischke, E. S., Hewson, J. H., Soja, A. J., Csiszar, I. A., Hyer, E. J., Loboda, T., Conrad, S. G., Romasko, V. I., Pavlichenko, E. A., Miskiv, S. I., & Slinkina, O. A. (2004). AVHRR-based mapping of fires in Russia: New products for fire management

and carbon cycle studies. *Remote Sensing of Environment*, *93*(4), 546–564. https://doi.org/10.1016/j.rse.2004.08.011

Talucci, A. C., Loranty, M. M., & Alexander, H. D. (2022). Siberian taiga and tundra fire regimes from 2001-2020. *Environmental Research Letters*, *17*. https://doi.org/10.1088/1748-9326/ac3f07

Turner, M. G., & Romme, W. H. (1994). Landscape dynamics in crown fire ecosystems. *Landscape Ecology*, *9*(1), 59–77. https://doi.org/DOI:10.1007/BF00135079

UNESCO (2023). National Park Kytalyk. https://whc.unesco.org/en/tentativelists/6520/. Accessed: 23.10.2023

University of Zurich. (2023). Mann-Whitney-U-Test. https://www.methodenberatung.uzh.ch/de/datenanalyse_spss/unterschiede/zentral/mann.html. Accessed: 25.04.2024

van Huissteden, J., Teshebaeva, K., Cheung, Y., Magnússon, R., Noorbergen, H., Karsanaev, S. V., Maximov, T. C., & Dolman, A. J. (2021). Geomorphology and InSAR-Tracked Surface Displacements in an Ice-Rich Yedoma Landscape. *Frontiers in Earth Science*, *9*(680565), 1–21. https://doi.org/10.3389/feart.2021.680565

Walker, D. A., Raynolds, M. K., Daniëls, F. J. A., Einarsson, E., Elvebakk, A., Gould, W. A., Katenin, A. E., Kholod, S. S., Markon, C. J., Melnikov, E. S., Moskalenko, N. G., Talbot, S. S., & Yurtsev, B. A. (2005). The Circumpolar Arctic Vegetation Map. *Journal of Vegetation Science*, *16*(3), 267–282. https://doi.org/DOI:10.1111/j.1654-1103.2005.tb02365.x

Weiss, A. D. (2001). Topographic Position and Landforms Analysis. In *Poster presentation, ESRI user conference, San Diego, CA* (Vol. 2000).

Wu, Z., He, H. S., Fang, L., Liang, Y., & Parsons, R. A. (2018). Wind speed and relative humidity influence spatial patterns of burn severity in boreal forests of northeastern China. *Annals of Forest Science*, *75*(3). https://doi.org/10.1007/s13595-018-0749-z

Wu, Z., He, H. S., Liang, Y., Cai, L., & Lewis, B. J. (2013). Determining Relative Contributions of Vegetation and Topography to Burn Severity from LANDSAT Imagery. *Environmental Management*, *52*(4), 821–836. https://doi.org/10.1007/s00267-013-0128-3

8 Appendix

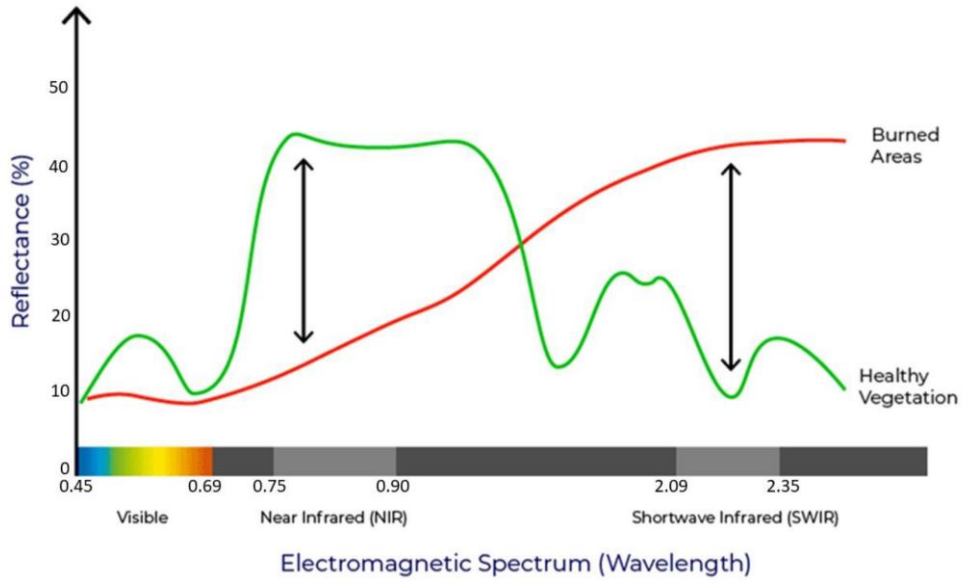

Figure 6: Spectral response of healthy vegetation compared to burned areas from Alcaras et al. (2022).

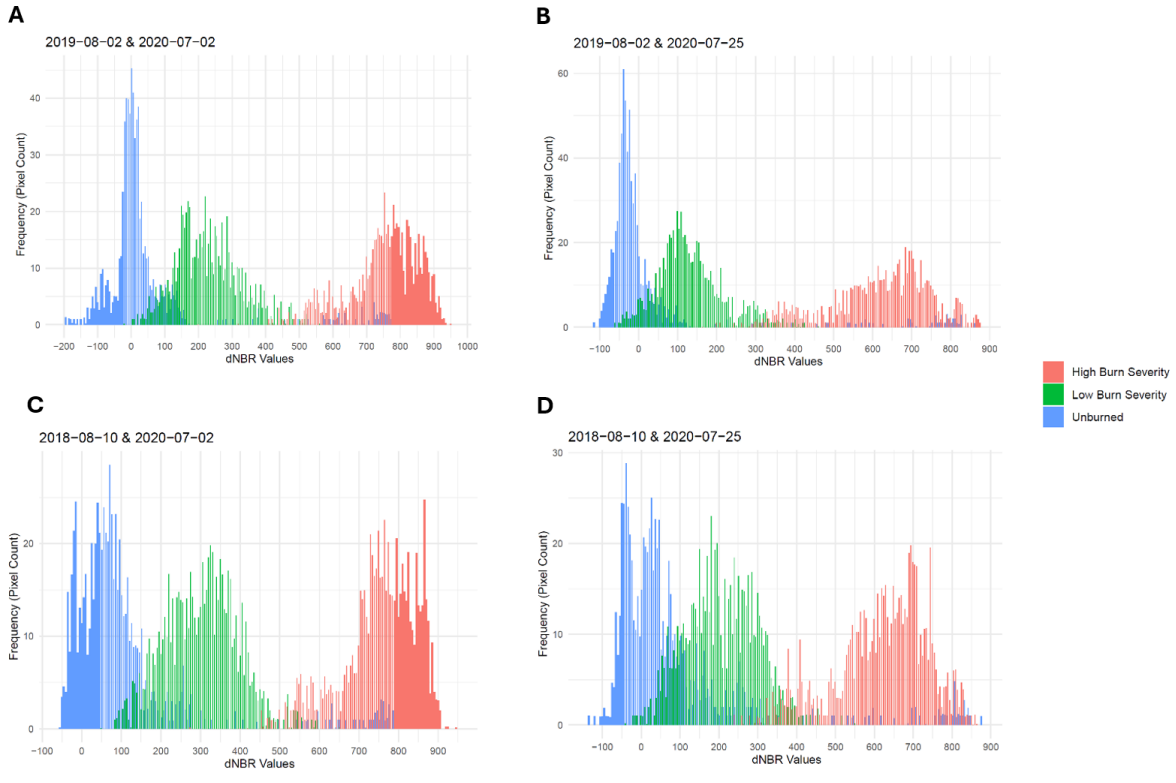

Figure 7: Histogram of the dNBR distributions from the training polygons for the three different burn severity classes (unburned, low burn severity and high burn severity) for different pre- and post-burn image combinations that were tested for the 2019 fire. A) Pre-burn image from 2019-08-02 and post-burn image from 2020-07-02. B) Pre-burn image from 2019-08-02 and post-burn image from 2020-07-25. C) pre-burn image from 2018-08-10 and post-burn image from 2020-07-02. D) Pre-burn image from 2018-08-10 and post-burn image from 2020-07-25.

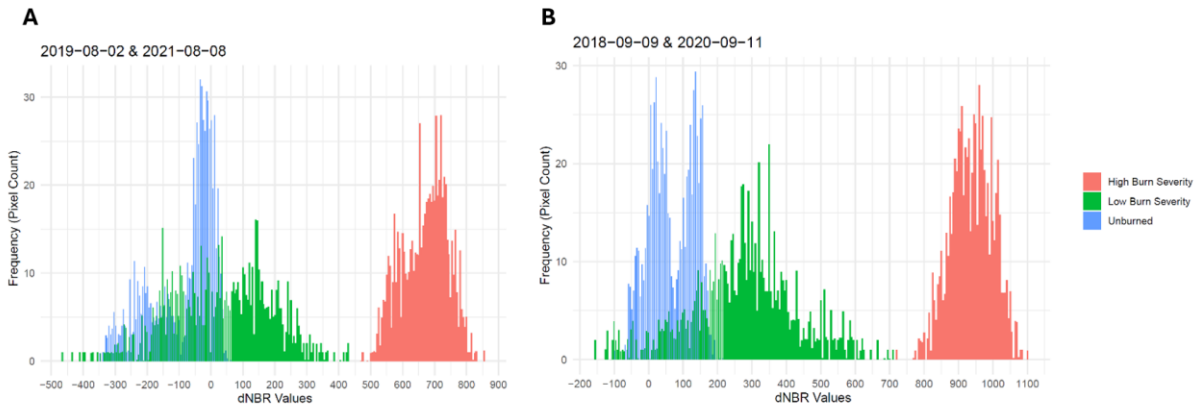

Figure 8: Histogram of the dNBR distributions from the training polygons for the three different burn severity classes (unburned, low burn severity and high burn severity) for different pre- and post-burn image combinations that were tested for the 2020 fire. A) Pre-burn image from 2019-08-02 and post-burn image from 2021-08-08. B) Pre-burn image from 2018-09-09 and post-burn image from 2020-09-11.

Table 6: Ordinal severity levels and the according example range of dNBR values (multiplied by 10^3) from Key & Benson (2006).

Severity level	dNBR range
Enhanced regrowth, high	–500 to –251
Enhanced regrowth, low	–250 to –101
Unburned	–100 to +99
Low severity	+100 to +269
Moderate-low severity	+270 to +439
Moderate-high severity	+440 to +659
High severity	+660 to +1300

A

		Predicted Values			
		High	**Low**	**Unburned**	**Total**
Actual Values	**High**	245	0	0	245
	Low	2	237	6	245
	Unburned	0	1	244	245
	Total	247	238	250	735

Overall Accuracy	(245+237+244)/735 = 98.776%	
	User's Accuracy	**Producer's Accuracy**
High	245/247 = 99.190%	245/245 = 100%
Low	237/238 = 99.580%	237/245 = 96.735%
Unburned	244/250 = 97.600%	244/245 = 99.592%

B

		Predicted Values			
		High	**Low**	**Unburned**	**Total**
Actual Values	**High**	245	0	0	245
	Low	0	128	117	245
	Unburned	0	13	232	245
	Total	245	141	349	735

Overall Accuracy	(245+128+232)/735 = 82.313%	
	User's Accuracy	**Producer's Accuracy**
High	245/245 = 100%	245/245 = 100%
Low	128/141 = 90.780%	128/245 = 52.245%
Unburned	232/349 = 66.476%	232/245= 94.694%

Figure 9: Confusion matrix with overall accuracy, user's accuracy and producer's accuracy for classification into high burn severity, low burn severity, and unburned area for A) the 2019 fire and B) 2020 fire.

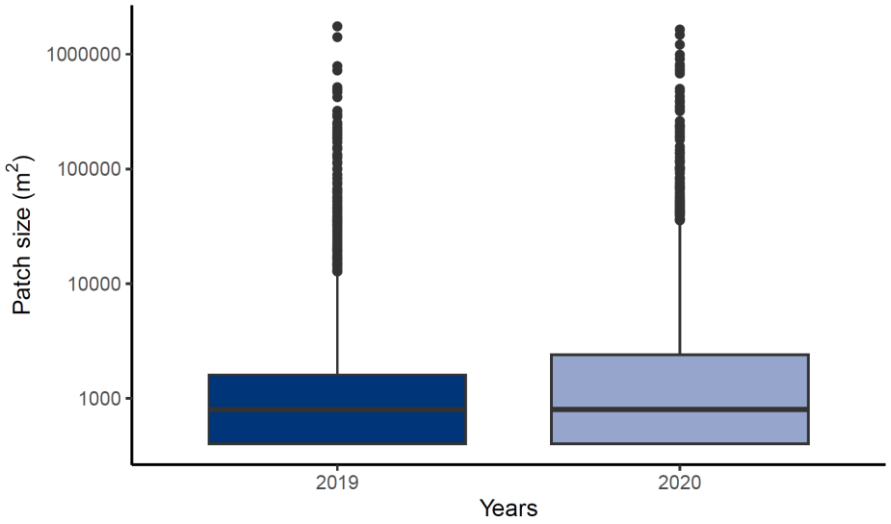

*Figure 10: Boxplot of the high burn severity patch sizes for the years 2019 and 2020. The black lines represent the median of each distribution. We sampled 2'000 data points in each year and log-transformed the patch size with base 10. We performed a Mann-Whitney-U test (statistic W = 1859687, p-value = 5.675 * 10^{-05}).*

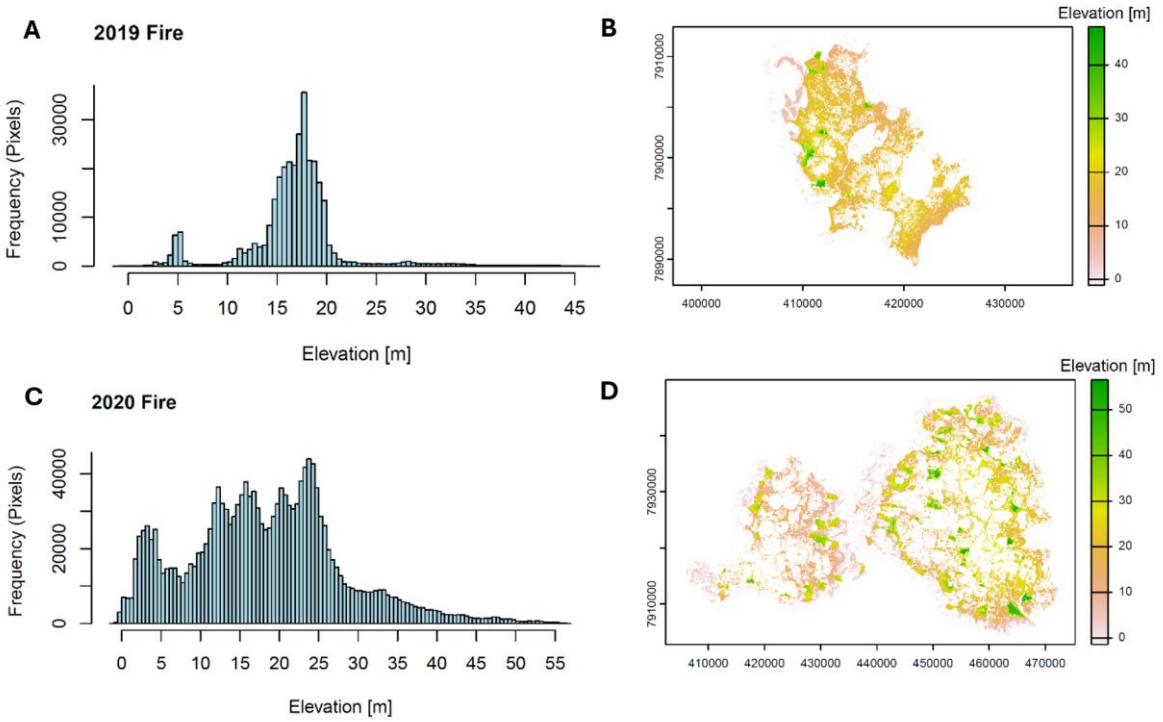

Figure 11: Histogram of all elevation values within the burned area of A) the 2019 fire and C) the 2020 fire. Elevation maps of B) the 2019 burned area and D) the 2020 burned area.

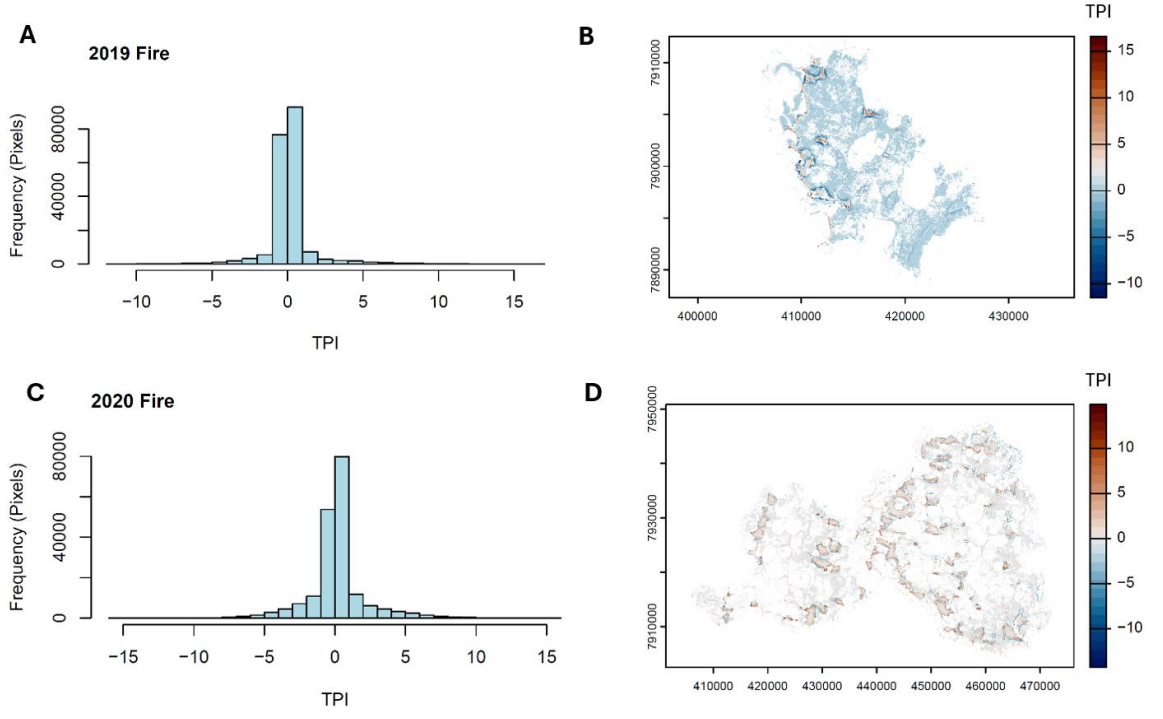

Figure 12: Histogram of all TPI values within the burned area of A) the 2019 fire and C) the 2020 fire. TPI maps of B) the 2019 burned area and D) the 2020 burned area.

Table 7: Generated elevation and TPI ranges for the 2019 and 2020 fire.

Elevation ranges for 2019 fire:	<5, 5-10, 10-15, …, 40-45
Elevation ranges for 2020 fire:	<5, 5-10, 10-15, …, 45-50, >50
TPI ranges for 2019 fire:	-10 to -5, -5 to -1, -1 to 1, 1 to 5, 5 to 10, 10 to 15
TPI ranges for 2020 fire:	-15 to -10, -10 to -5, -5 to -1, -1 to 1, 1 to 5, 5 to 10, 10 to 15

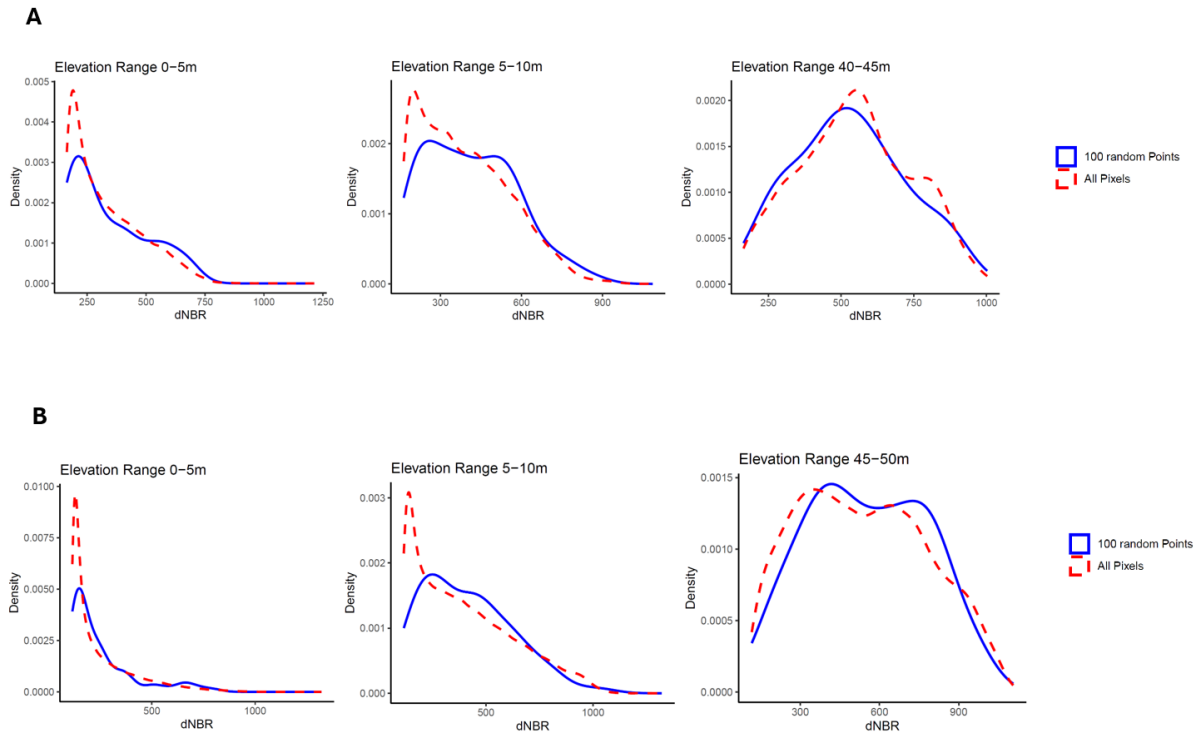

Figure 13: Elevation representativeness plots for A) the 2019 fire and B) the 2020 fire. All pixels within the elevation range were plotted against a sample of 100 random points within that respective elevation range.

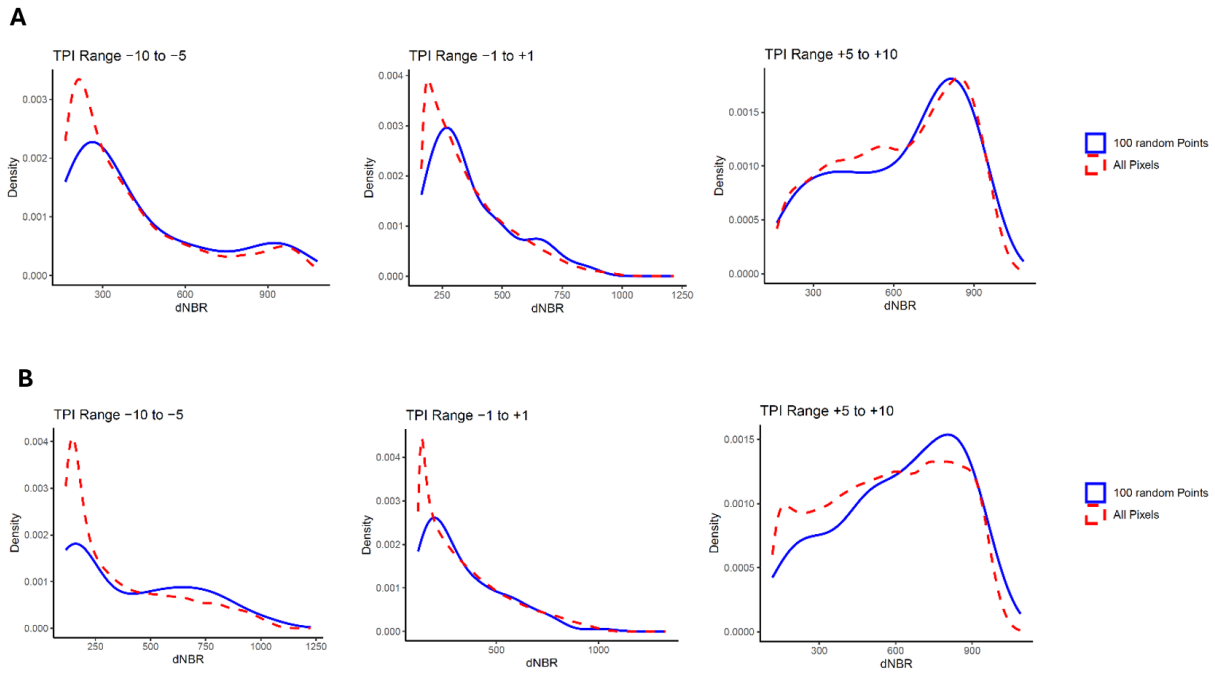

Figure 14: TPI representativeness plots for A) the 2019 fire and B) the 2020 fire. All pixels within the TPI range were plotted against a sample of 100 random points within that respective TPI range.

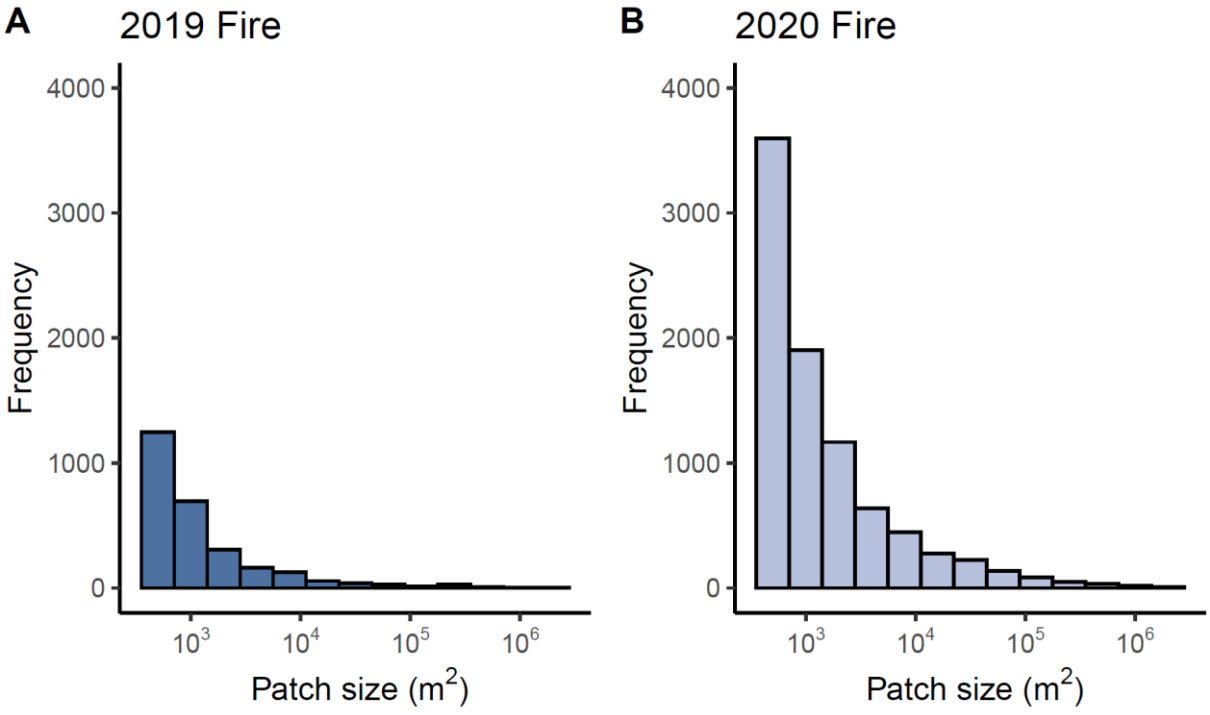

Figure 15: Frequency distribution of the high burn severity patch sizes for the two fire scars A) 2019 and B) 2020.

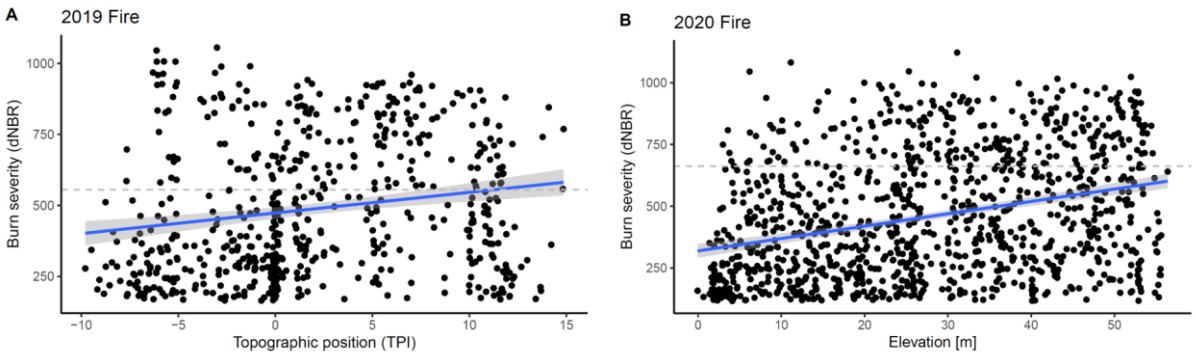

*Figure 16: A) Relation between burn severity (dNBR) and TPI and B) burn severity (dNBR) and elevation. The black dots represent random samples within the fire scars. The blue lines show the linear regression line fitted to the data with a confidence interval (R^2 = 0.03173, p-value = 1.136 * 10^{-5} for A) and R^2 = 0.09873, p-value = < 2.2 * 10^{-16} for B). The grey dashed lines illustrate the thresholds between low and high burn severity (dNBR threshold at 555 for A) and dNBR threshold at 662 for B).*

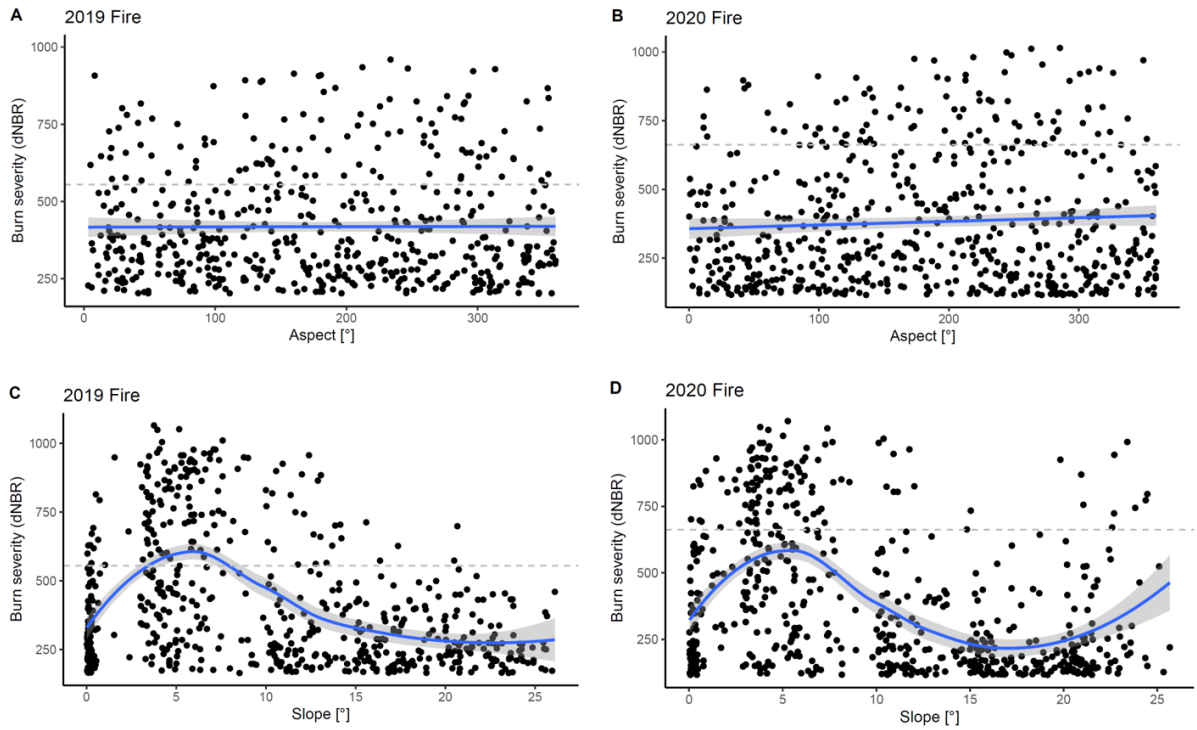

*Figure 17: Relation between burn severity (dNBR) and aspect for A) the 2019 fire and B) the 2020 fire, and relation between burn severity (dNBR) and slope for C) the 2019 fire and D) the 2020 fire. The blue lines in A) and B) show the linear regression line fitted to the data with a confidence interval (R^2 = 9.124 * 10^{-5}, p-value = 0.8154 for A) and R^2 = 0.003476, p-value = 0.1492 for B). The blue lines in C) and D) show the visual trendline with confidence interval with the loess method, as the assumptions for a linear model were not met. The black dots represent random samples within the fire scars. The grey dashes lines illustrate the thresholds between low and high burn severity (dNBR threshold at 555 for A) and C) and dNBR threshold at 662 for B) and D). We calculated the slope and aspect with the RStudio terrain package, using four neighbouring cells for the computation.*

Figure 18: Picture of the Siberian tundra fires in 2019 shot from an airplane from Nicole Zweifel.

9 Personal Declaration

I hereby declare that the submitted thesis is the result of my own, independent work. All external sources are explicitly acknowledged in the thesis.

Staufen, 30. April 2024

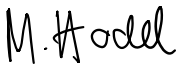

Melanie Hodel